

# Tensor Full Feature Measure and Its Nonconvex Relaxation Applications to Tensor Recovery

Hongbing Zhang, Xinyi Liu, Hongtao Fan, Yajing Li, Yinlin Ye

**Abstract**—Tensor sparse modeling, as a promising method, has achieved great success in the whole field of science and engineering. As is known to all, various data in practical application are often generated by multiple factors, so the use of tensors to represent the data containing the internal structure of multiple factors came into being. However, different from the matrix case, constructing reasonable sparse measure of tensor is a relatively difficult and very important task. In this paper, we propose a novel tensor sparsity measure called Tensor Full Feature Measure (FFM). It comprehensively delineates the sparse features of tensors by simultaneously integrating the feature information of each dimension of tensors and the relevant feature information between any two different dimensions, and for the first time relates Tucker rank to tensor tube rank, which further advances the connection between the definitions of tensor rank. On this basis, we establish its non-convex relaxation, and apply FFM to two typical problems of tensor recovery: low-rank tensor completion (LRTC) and tensor robust principal component analysis (TRPCA). LRTC and TRPCA models based on FFM are proposed, and two efficient Alternating Direction Multiplier Method (ADMM) algorithms are developed to solve the proposed model. A variety of real numerical experiments substantiate the superiority of the proposed methods beyond state-of-the-arts.

**Index Terms**—Tensor sparsity, Tensor rank, Tucker rank, Tubal rank, Nonconvex optimization, Alternating direction method of multipliers (ADMM), Image recovery.



## 1 INTRODUCTION

TENSOR play an increasingly important role in many applications, such as hyperspectral/multispectral image (HSI/MSI) processing [1], [2], [3], [4], color image/video (CI/CV) processing [5], [6], [7], [8], magnetic resonance imaging (MRI) data recovery [9], [10], [11], [12], background subtraction [13], [14], [15], [16], video rain stripe removal [17], [18] and signal reconstruction [19], [20]. These applications can often be expressed as tensor recovery problems, that is, recovering underlying tensors from damaged observations. In particular, as two typical examples, tensor robust principal component analysis aims to eliminate sparse outliers, and tensor completeness aims to complete missing elements. The key of tensor recovery is to explore the sparse feature of underlying tensors. Therefore, in the process of tensor recovery, it is very important to consider an appropriate quantitative measure of tensor sparsity. Specifically, the tensor recovery model based on sparsity can usually be expressed as follows:

$$\min_{\mathcal{X}} S(\mathcal{X}) + \gamma L(\mathcal{X}, \mathcal{Y}), \quad (1)$$

where  $\mathcal{Y} \in \mathbb{R}^{I_1 \times I_2 \times \dots \times I_N}$  is the observation,  $L(\mathcal{X}, \mathcal{Y})$  is the loss function between  $\mathcal{X}$  and  $\mathcal{Y}$ ,  $S(\mathcal{X})$  defines the tensor sparsity

measure of  $\mathcal{X}$  and  $\gamma$  is the compromise parameter. It is easy to see that the key problem in constructing (1) is to design an appropriate tensor sparsity measure on data.

As we all know, tensors are high-order generalizations of matrices. Matrix can be reasonably measured by the quantity (ranks) of nonzero singular values. Its relaxed form (nuclear norm) has been proven to be helpful for fine coding of data sparseness in applications, and has inspired various low-rank models and algorithms for different practical problems [21], [22], [23], [24], [25], [26], [27], [28]. But the sparsity of tensors cannot be quantitatively measured according to the rank of matrices. The main reason is that there is no unique definition of the rank of a tensor. In the past few decades, the most popular rank definitions are CANDECOMP/PARAFAC(CP) rank based on CP decomposition [29], [30], Tucker rank based on Tucker decomposition [31], [32] and tubal-rank and multi-rank [33] based on t-svd. Calculating CP rank of a given tensor is NP hard [34], which makes its application quite inconvenient. Tucker rank is often directly extended to higher order by simply finding the rank (or its relaxation) of all tensor mode unfolding matrices. However, such simple rank-sum terms do not fully represent the feature of tensors. To be specific, the properties of tensor sparse measures should surpass the low-rank properties of all unfolding matrices according to modes, rather than simply considering the low-rank properties of each mode. The t-SVD was first proposed by Braman et al. [35] and Kilmer et al. [36], based on the tensor-tensor product, in which the third-order tensor is integrated to avoid the loss of information inherent in the matrixization or flattening of the tensor [37]. However, the limitation of its tensor-tensor product makes it impossible to apply to higher-order situations. In [38] Zheng et al. proposed a new rank (N-tubal rank), in the form of the higher-order tensor

- This work was supported by the National Natural Science Foundation of China (Nos. 11701456, 11801452), Fundamental Research Project of Natural Science in Shaanxi Province General Project (Youth) (Nos. 2019JQ-415, 2019JQ-196), the Initial Foundation for Scientific Research of Northwest A&F University (Nos.2452017219, 2452018017), and Innovation and Entrepreneurship Training Program for College Students of Shaanxi Province (S201910712132).
- H. Zhang, X. Liu, H. Fan, Y. Li and Y. Ye are with the College of Science, Northwest A&F University, Yangling, Shaanxi 712100, China (e-mail: zhanghb@nwfufu.edu.cn; Lxy6x1@163.com; fanht17@nwfufu.edu.cn; hlijyajing@163.com; 13314910376@163.com).

using the new way will unfold into multiple three-order tensor, in this way t-SVD is applied to the situation of the higher order. However, based on the tubal rank obtained by t-SVD, the feature shown tend to be more inclined to the relevant feature of the first and the second dimensions of the three-order tensor. N-tube rank adopts t-SVD of multiple three-order tensors, and obtains the correlation feature between any two dimensions. But it still has certain defects in the sparse features of tensors, i.e., it lacks a feature information of each dimension itself. Actually, color video data contains four dimensions, one of which is time, and time has continuity and a feature information of its own. Considering only about the relationship between two dimensions misses the character of each dimension itself. Therefore, it is necessary to find a sparse measure with comprehensiveness.

## 1.1 OUR CONTRIBUTION

In response to the above problems, this article mainly made four contributions.

Firstly, we propose for the first time a tensor sparse measure that can represent all the feature information of a tensor. In order to describe its unique feature aptly, we name it as full feature measure (FFM). This new measure not only contains the feature information of each dimension and the relevant information features between any two different dimensions, but also integrates Tucker rank and tube rank for the first time and draws on the advantages of the two kinds of rank, thus further advancing the connection between different rank definitions.

Secondly, in response to the above problem, a type of sparsity measure minimization model, which is an NP-hard problem, is established. To address such problem, a relaxed form based on FFM is developed. In the FFM relaxation process, since the sparse measure we proposed is a non-convex function, the accuracy of our method will be greatly reduced if only the traditional kernel norm convex relaxation is adopted. In order to further sharply improve the accuracy and efficiency of such model, we propose a type of non-convex relaxation form of FFM.

Thirdly, by applying FFM to two typical tensor recovery problems, a tensor complete model based on FFM (FFMTC) and a tensor robust principal component analysis model based on FFM (FFMTRPCA) are proposed respectively. Meanwhile, two efficient Alternate Direction Multiplier Method (ADMM) algorithms are designed and used to solve the FFM-based tensor complete minimization problem and the FFM-based tensor robust principal component analysis problem respectively. On this basis, the closed solution of each parameter update is obtained, which facilitates the effective implementation of the presented algorithm.

Fourth, for the low-rank tensor completeness problem, we apply the proposed FFMTC model to a variety of real data tasks, including multispectral image, magnetic resonance imaging, color video and hyperspectral video. In these four experiments with real data, our method is the optimal method compared with state-of-the-art methods, and has obvious improvement compared with the sub-optimal method. In particular, the model can still achieve excellent results when the sampling rate is low. For tensor robust principal component analysis, we apply the proposed

FFMTRPCA model to the task of restoring hyperspectral data damaged by salt and pepper noise. As we all know, salt and pepper noise is quite serious for image damage. However, when the noise level reaches 0.4, our method can still achieve excellent results in retaining original information and removing noise. A variety of experiments prove that our method is more comprehensive and efficient than other state-of-the-art methods. Through experiments on various real data, the convergence behavior of the algorithm in ADMM framework is obtained. Experiments show that our algorithm can converge quickly and ensure the effectiveness of the algorithm. In summary, the proposed model behaves extremely effective and fairly efficient.

The rest of this paper is structured as follows. Section 2 gives some notations and preliminaries. Section 3 introduces some related work on tensor sparse measure. Section 4 provides our approach and its relaxation. Section 5 supplies two models and algorithms for solving LRTC and TRPCA problems. Section 6 presents numerical experiments conducted on real data. We conclude this work in Section 7.

## 2 NOTATIONS AND PRELIMINARIES

In this section, we give some basic notations and briefly introduce some definitions used throughout the paper. Generally, a lowercase letter and an uppercase letter denote a vector  $x$  and a matrix  $X$ , respectively. An  $N$ -th order tensor is denoted by a calligraphic upper case letter  $\mathcal{X} \in \mathbb{R}^{I_1 \times I_2 \times \dots \times I_N}$  and  $x_{i_1, i_2, \dots, i_N}$  is its  $(i_1, i_2, \dots, i_N)$ -th element. The Frobenius norm of a tensor is defined as  $\|\mathcal{X}\|_F = (\sum_{i_1, i_2, \dots, i_N} x_{i_1, i_2, \dots, i_N}^2)^{1/2}$ . For a three order tensor  $\mathcal{X} \in \mathbb{R}^{I_1 \times I_2 \times I_3}$ . We use  $\tilde{\mathcal{X}}$  to denote the tensor generated by performing discrete Fourier transformation (DFT) along each tube of  $\mathcal{X}$ , i.e.,  $\tilde{\mathcal{X}} = \text{fft}(\mathcal{X}, [], 3)$ . The inverse DFT is computed by command  $\text{ifft}$  satisfying  $\mathcal{X} = \text{ifft}(\tilde{\mathcal{X}}, [], 3)$ . More often, the frontal slice  $\mathcal{X}(:, :, i)$  is denoted compactly as  $\mathcal{X}^{(i)}$ .

**Definition 1 (Tensor Mode- $n$  Unfolding and Folding [39]).**

The mode- $n$  unfolding of a tensor  $\mathcal{X} \in \mathbb{R}^{I_1 \times I_2 \times \dots \times I_N}$  is denoted as a matrix  $\mathcal{X}_{(n)} \in \mathbb{R}^{I_n \times I_1 \dots I_{n-1} I_{n+1} \dots I_N}$ . Tensor element  $(i_1, i_2, \dots, i_N)$  maps to matrix element  $(i_n, j)$ , where

$$j = 1 + \sum_{k=1, k \neq n}^N (i_k - 1) J_k \quad \text{with} \quad J_k = \prod_{m=1, m \neq n}^{k-1} I_m. \quad (2)$$

The mode- $n$  unfolding operator and its inverse are respectively denoted as  $\text{unfold}_n$  and  $\text{fold}_n$ , and they satisfy  $\mathcal{X} = \text{fold}_n(\mathcal{X}_{(n)}) = \text{fold}_n(\text{unfold}_n(\mathcal{X}))$ .

**Definition 2 (The mode- $n$  product of tensor [39]).**

The mode- $n$  product of tensor  $\mathcal{X} \in \mathbb{R}^{I_1 \times I_2 \times \dots \times I_N}$  with matrix  $U \in \mathbb{R}^{J_n \times I_n}$  is denoted by  $\mathcal{Y} = \mathcal{X} \times_n U$ , where  $\mathcal{Y} \in \mathbb{R}^{I_1 \times I_2 \times \dots \times I_{n-1} I_{n+1} \dots \times I_N}$ . Elementwise, we have

$$\mathcal{Y} = \mathcal{X} \times_n U \quad \Leftrightarrow \quad \mathcal{Y}_{(n)} = U \cdot \text{unfold}_n(\mathcal{X}_{(n)}). \quad (3)$$

**Definition 3 (Mode- $k_1 k_2$  slices [38]).**

For an  $N$ -th order tensor  $\mathcal{X} \in \mathbb{R}^{I_1 \times I_2 \times \dots \times I_N}$ , its mode- $k_1 k_2$  slices  $(\mathcal{X}^{(k_1 k_2)})$ ,  $1 \leq k_1 < k_2 \leq N$ ,  $k_1, k_2 \in \mathbb{Z}$  are two-dimensional sections, defined by fixing all but the mode- $k_1$  and the mode- $k_2$  indexes.

**Definition 4 (Tensor Mode- $k_1, k_2$  Unfolding and Folding [38]).**

For an  $N$ -th order tensor  $\mathcal{X} \in \mathbb{R}^{I_1 \times I_2 \times \dots \times I_N}$ , its

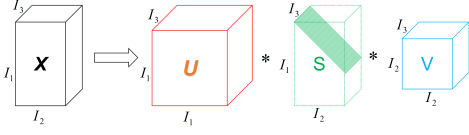


Fig. 1. An illustration of the t-SVD of an  $I_1 \times I_2 \times I_3$  tensor

mode- $k_1 k_2$  unfolding is a three order tensor denoted by  $\mathcal{X}_{(k_1 k_2)} \in \mathbb{R}^{I_{k_1} \times I_{k_2} \times \prod_{s \neq k_1, k_2} I_s}$ , the frontal slices of which are the lexicographic orderings of the mode- $k_1 k_2$  slices of  $\mathcal{X}$ . Mathematically, the  $(i_1, i_2, \dots, i_N)$ -th element of  $\mathcal{X}$  maps to the  $(i_{k_1}, i_{k_2}, j)$ -th element of  $\mathcal{X}_{(k_1 k_2)}$ , where

$$j = 1 + \sum_{s=1, s \neq k_1, s \neq k_2}^N (i_s - 1) J_s \quad \text{with} \quad J_s = \prod_{m=1, m \neq k_1, m \neq k_2}^{s-1} I_m. \quad (4)$$

The mode- $k_1 k_2$  unfolding operator and its inverse operation are respectively denoted as  $\mathcal{X}_{(k_1 k_2)} := t - \text{unfold}(\mathcal{X}, k_1, k_2)$  and  $\mathcal{X} := t - \text{fold}(\mathcal{X}_{(k_1 k_2)}, k_1, k_2)$ .

For a three order tensor  $\mathcal{X} \in \mathbb{R}^{I_1 \times I_2 \times I_3}$ , the block circulation operation is defined as

$$\text{bcirc}(\mathcal{X}) := \begin{pmatrix} X^{(1)} & X^{(I_3)} & \dots & X^{(2)} \\ X^{(2)} & X^{(1)} & \dots & X^{(3)} \\ \vdots & \vdots & \ddots & \vdots \\ X^{(I_3)} & X^{(I_3-1)} & \dots & X^{(1)} \end{pmatrix} \in \mathbb{R}^{I_1 I_3 \times I_2 I_3}.$$

The block diagonalization operation and its inverse operation are defined as

$$\text{bdiag}(\mathcal{X}) := \begin{pmatrix} X^{(1)} & & & \\ & X^{(2)} & & \\ & & \ddots & \\ & & & X^{(I_3)} \end{pmatrix} \in \mathbb{R}^{I_1 I_3 \times I_2 I_3},$$

$$\text{bdfold}(\text{bdiag}(\mathcal{X})) := \mathcal{X}.$$

The block vectorization operation and its inverse operation are defined as

$$\text{bvec}(\mathcal{X}) := \begin{pmatrix} X^{(1)} \\ X^{(2)} \\ \vdots \\ X^{(I_3)} \end{pmatrix} \in \mathbb{R}^{I_1 I_3 \times I_2}, \quad \text{bvfold}(\text{bvec}(\mathcal{X})) := \mathcal{X}.$$

**Definition 5 (T-product [40]).** Let  $\mathcal{A} \in \mathbb{R}^{I_1 \times I_2 \times I_3}$  and  $\mathcal{B} \in \mathbb{R}^{I_2 \times J \times I_3}$ . Then the t-product  $\mathcal{A} * \mathcal{B}$  is defined to be a tensor of size  $I_1 \times J \times I_3$ ,

$$\mathcal{A} * \mathcal{B} := \text{bvfold}(\text{bcirc}(\mathcal{A}) \text{bvec}(\mathcal{B})).$$

Since that circular convolution in the spatial domain is equivalent to multiplication in the Fourier domain, the T-product between two tensors  $\mathcal{C} = \mathcal{A} * \mathcal{B}$  is equivalent to

$$\tilde{\mathcal{C}} = \text{bdfold}(\text{bdiag}(\tilde{\mathcal{A}}) \text{bdiag}(\tilde{\mathcal{B}})).$$

**Definition 6 (Tensor conjugate transpose [40]).** The conjugate transpose of a tensor  $\mathcal{A} \in \mathbb{C}^{I_1 \times I_2 \times I_3}$  is the tensor  $\mathcal{A}^H \in \mathbb{C}^{I_2 \times I_1 \times I_3}$  obtained by conjugate transposing each

### Algorithm 1 t-SVD [41]

**Input:**  $\mathcal{X} \in \mathbb{R}^{I_1 \times I_2 \times I_3}$

**Output:** t-SVD components  $\mathcal{U}$ ,  $\mathcal{S}$  and  $\mathcal{V}$  of  $\mathcal{A}$ .

- 1: Compute  $\tilde{\mathcal{A}} = \text{fft}(\mathcal{A}, [], 3)$ .
  - 2: Compute each frontal slice of  $\tilde{\mathcal{U}}$ ,  $\tilde{\mathcal{S}}$ , and  $\tilde{\mathcal{V}}$  from  $\tilde{\mathcal{A}}$  by
  - 3: **for**  $i = 1, \dots, \lfloor \frac{I_3+1}{2} \rfloor$  **do**
  - 4:    $[\tilde{\mathcal{U}}^{(i)}, \tilde{\mathcal{S}}^{(i)}, \tilde{\mathcal{V}}^{(i)}] = \text{SVD}(\tilde{\mathcal{A}}^{(i)})$ ;
  - 5: **end for**
  - 6: **for**  $i = \lfloor \frac{I_3+1}{2} \rfloor + 1, \dots, I_3$  **do**
  - 7:    $[\tilde{\mathcal{U}}^{(i)}, \tilde{\mathcal{S}}^{(i)}, \tilde{\mathcal{V}}^{(i)}] = \text{SVD}(\tilde{\mathcal{A}}^{(i)})$ ;
  - 8:    $\tilde{\mathcal{U}}^{(i)} = \text{conj}(\tilde{\mathcal{U}}^{(I_3-i+2)})$ ;
  - 9:    $\tilde{\mathcal{S}}^{(i)} = \tilde{\mathcal{S}}^{(I_3-i+2)}$ ;
  - 10:    $\tilde{\mathcal{V}}^{(i)} = \text{conj}(\tilde{\mathcal{V}}^{(I_3-i+2)})$ ;
  - 11: **end for**
- Compute  $\mathcal{U} = \text{ifft}(\tilde{\mathcal{U}}, [], 3)$ ,  $\mathcal{S} = \text{ifft}(\tilde{\mathcal{S}}, [], 3)$ , and  $\mathcal{V} = \text{ifft}(\tilde{\mathcal{V}}, [], 3)$ .

of the frontal slices and then reversing the order of transposed frontal slices 2 through  $I_3$ .

**Definition 7 (identity tensor [40]).** The identity tensor  $\mathcal{I} \in \mathbb{R}^{I_1 \times I_1 \times I_3}$  is the tensor whose first frontal slice is the  $I_1 \times I_1$  identity matrix, and whose other frontal slices are all zeros.

It is clear that  $\text{bcirc}(\mathcal{I})$  is the  $I_1 I_3 \times I_1 I_3$  identity matrix. So it is easy to get  $\mathcal{A} * \mathcal{I} = \mathcal{A}$  and  $\mathcal{I} * \mathcal{A} = \mathcal{A}$ .

**Definition 8 (orthogonal tensor [40]).** A tensor  $\mathcal{Q} \in \mathbb{R}^{I_1 \times I_1 \times I_3}$  is orthogonal if it satisfied

$$\mathcal{Q} * \mathcal{Q}^H = \mathcal{Q}^H * \mathcal{Q} = \mathcal{I}.$$

**Definition 9 (F-diagonal Tensor [40]).** A tensor is called f-diagonal if each of its frontal slices is a diagonal matrix.

**Theorem 1 (t-SVD [41]).** Let  $\mathcal{X} \in \mathbb{R}^{I_1 \times I_2 \times I_3}$  be a three order tensor, then it can be factored as

$$\mathcal{X} = \mathcal{U} * \mathcal{S} * \mathcal{V}^H,$$

where  $\mathcal{U} \in \mathbb{R}^{I_1 \times I_1 \times I_3}$  and  $\mathcal{V} \in \mathbb{R}^{I_2 \times I_2 \times I_3}$  are orthogonal tensors, and  $\mathcal{S} \in \mathbb{R}^{I_1 \times I_2 \times I_3}$  is an f-diagonal tensor. The t-SVD scheme is illustrated in Fig.1, and its computation is given in Algorithm 1.

**Definition 10 (tensor tubal-rank and multi-rank [33]).** The tubal-rank of a tensor  $\mathcal{X} \in \mathbb{R}^{I_1 \times I_2 \times I_3}$ , denoted as  $\text{rank}_t(\mathcal{X})$ , is defined to be the number of non-zero singular tubes of  $\mathcal{S}$ , where  $\mathcal{S}$  comes from the t-SVD of  $\mathcal{X} : \mathcal{X} = \mathcal{U} * \mathcal{S} * \mathcal{V}^H$ . That is

$$\text{rank}_t(\mathcal{X}) = \#\{i : \mathcal{S}(i, :, :) \neq 0\}. \quad (5)$$

The tensor multi-rank of  $\mathcal{X} \in \mathbb{R}^{I_1 \times I_2 \times I_3}$  is a vector, denoted as  $\text{rank}_r(\mathcal{X}) \in \mathbb{R}^{I_3}$ , with the  $i$ -th element equals to the rank of  $i$ -th frontal slice of  $\mathcal{X}$ .

## 3 RELATED WORK

In this section, we first review some sparsity-based tensor recovery methods proposed in previous literatures, and then briefly review two particular sparse measure, both containing insightful understanding of tensor sparsity.

### 3.1 Tucker rank

The Tucker rank is defined as a vector, the  $i$ -th element of which is the rank of the mode- $i$  unfolding matrix [42], i.e.,

$$\text{rank}_{t_c} := (\text{rank}(\mathcal{X}_{(1)}), \text{rank}(\mathcal{X}_{(2)}), \dots, \text{rank}(\mathcal{X}_{(N)})) \quad (6)$$

where  $\mathcal{X}$  is an  $N$ -order tensor and  $\mathcal{X}_{(i)}$  ( $i = 1, 2, \dots, N$ ) is the mode- $i$  unfolding of  $\mathcal{X}$ . In order to facilitate the minimization of the Tucker rank, Liu et al. [43] considered its convex relaxation, defined as the sum of the nuclear norm (SNN) of unfolding matrices, i.e.,

$$\|\mathcal{X}\|_{SNN} = \sum_{i=1}^N \alpha_i \|\mathcal{X}_{(i)}\|_*, \quad (7)$$

where  $\mathcal{X} \in \mathbb{R}^{I_1 \times I_2 \times \dots \times I_N}$ ,  $\mathcal{X}_{(i)}$  is unfolding the tensor along the  $i$ -th dimension, and  $\|\cdot\|_*$  is the nuclear norm of a matrix, i.e., sum of singular values. This simple calculation algorithm makes SNN widely used [9], [44], [45], [46]. Although SNN can flexibly make use of features along different modes by adjusting the weights  $\alpha_i$  [47], such models that expand directly along each dimension are often inadequate in describing the sparsity of tensors. Because unfolding tensor into matrices will inevitably destroy the internal structure of the tensor, which will cause loss of information. For example, unfolding a CV along its temporal dimension damages the spatial information of each frame in the CV. And each unfolding matrix only contains the feature information of each dimension, ignoring the intrinsic correlation between tensor dimensions.

### 3.2 tensor nuclear norm

To avoid information loss in SNN, Kilmer and Martin [40] propose a tensor decomposition named t-SVD with a Fourier transform matrix. Zhang et al. [33] proposed tensor tubal-rank and tensor multi-rank based on t-SVD. Directly minimizing the tensor tubal/multi-rank is NP-hard [34], so Zhang et al. [33] give a definition of the tensor nuclear norm on  $\mathcal{X} \in \mathbb{R}^{I_1 \times I_2 \times I_3}$  corresponding to t-SVD, i.e., Tensor Nuclear Norm (TNN):

$$\|\mathcal{X}\|_{TNN} := \sum_{i=1}^{I_3} \|\bar{\mathcal{X}}^{(i)}\|_*, \quad (8)$$

where  $\bar{\mathcal{X}}^{(i)}$  is the  $i$ -th frontal of  $\bar{\mathcal{X}}$ , with  $\bar{\mathcal{X}} = \text{fft}(\mathcal{X}, [], 3)$ . The operation of Fourier transform along the third dimension makes TNN based models have a natural computing advantage for video and other data with strong time continuity along a certain dimension. Although TNN is very effective in maintaining the internal structure of tensors, It's easy to find obvious two shortcomings. One is that it cannot be applied to higher-order ( $N > 3$ ) applications, because t-SVD limits its application to a three-order tensor. The other is that it lacks different correlations under different modes. In the t-SVD framework, for the three-order tensor, the correlations of the first and second dimensions are represented by matrix singular values, while the features of the third dimension are generated by embedded cyclic convolution. Therefore, TNN tends to highlight the correlation between the first and second dimensions. In view of this, Zheng et al. [38] proposed n-tubal rank to remedy the above defects.

**Definition 11 (n-tubal rank [38]).** The tensor n-tubal rank is a vector consisting of the tubal ranks of all mode- $k_1 k_2$  ( $k_1 \neq k_2$ ) unfolding tensors, i.e.,

$$\begin{aligned} N - \text{rank}_t(\mathcal{X}) := & (\text{rank}_t(\mathcal{X}_{12}), \text{rank}_t(\mathcal{X}_{13}), \dots, \\ & \text{rank}_t(\mathcal{X}_{1N}), \text{rank}_t(\mathcal{X}_{23}), \dots, \text{rank}_t(\mathcal{X}_{2N}), \dots, \\ & \text{rank}_t(\mathcal{X}_{N-1N})) \in \mathbb{R}^{N(N-1)/2}. \end{aligned} \quad (9)$$

It is not difficult to find that n-tube rank makes up for the defect of TNN, and its feature is the correlation between any two dimensions. However, it is still not sufficient to express the correlation between any two dimensions of a tensor, and the feature of each dimension are of vital importance. For example, the time dimension in the video has a certain correlation with the space dimension, but its unique feature in time cannot be ignored. The specific experimental results can be found in the experimental section, and there is a lot of room for improvement from its observation.

To be inspired by this and to solve this very difficult problem right now, we attempt to propose a measure for more reasonable and comprehensive assessing tensor sparsity.

## 4 TENSOR FULL FEATURE MEASURE AND RELAXATION

### 4.1 Tensor Full Feature Measure

Through more fully consider the properties of Tucker rank and N-tubal rank comprehensively, the full feature measure (FFM) of the proposed tensor  $\mathcal{X}$  has the following expression:

$$S(\mathcal{X}) = \sum_{1 \leq k_1 \leq k_2 \leq N} \beta_{k_1 k_2} \text{rank}(\mathcal{X}_{(k_1 k_2)}) \quad (10)$$

where parameter  $\beta_{k_1 k_2} \geq 0$  ( $1 \leq k_1 \leq k_2 \leq N, k_1, k_2 \in \mathbb{Z}$ ) and  $\sum_{1 \leq k_1 \leq k_2 \leq N} \beta_{k_1 k_2} = 1$  and  $\mathcal{X}_{(k_1 k_2)} = \text{unfold}_{k_1}(\mathcal{X})$  ( $k_1 = k_2$ ),  $\mathcal{X}_{(k_1 k_2)} = t - \text{unfold}(\mathcal{X}, k_1, k_2)$  ( $k_1 \neq k_2$ ). It is not difficult to find that (10) can be divided into two parts. The first part is  $k_1 = k_2$ , which mainly delivers the feature information of each dimension. The second part is  $k_1 \neq k_2$ , which can convey the feature information of the correlation between any two different dimensions. The weight parameter  $\beta_{k_1 k_2}$  is used to balance the size difference between the different ranks, so that the different ranks of different representations are equal. This comprehensive consideration makes the tensor not only has the internal correlation of any two dimensions, but also contain the low-rank property of the tensor space along each mode, so that the tensor sparsity can be described more fully.

### 4.2 Relaxation

It should be noted that the rank term in (10) can only take discrete values, which will produce optimization problems that are difficult to solve in practical applications [48]. However, directly using the nuclear norm as its loose approximation will still have a considerable gap with the original rank minimization problem, which usually leads to excessive punishment of the optimization problem and sub-optimality of the original problem solution. To remedy this shortcoming, we therefore exploit non-convex relaxation

---

**Algorithm 2** FFMTC
 

---

**Input:** an incomplete tensor  $\mathcal{Z}$ , the index set of the known elements  $\Omega$ , convergence criteria  $\epsilon$ , maximum iteration number  $K$ .

**Initialization:**  $\mathcal{X}^0 = \mathcal{Z}_\Omega$ ,  $\mathcal{M}_{k_1 k_2}^0 = \mathcal{X}^0$ ,  $\mu_{k_1 k_2}^0 > 0$ ,  $\rho > 1$ .

- 1: **while** not converged and  $k < K$  **do**
- 2:   Updating  $\mathcal{M}_{k_1 k_2}^k$  via (25);
- 3:   Updating  $\mathcal{X}^k$  via (27);
- 4:   Updating the multipliers  $\mathcal{Q}_{k_1 k_2}^k$  via (28);
- 5:    $\mu_{k_1 k_2}^k = \rho \mu_{k_1 k_2}^{k-1}$ ,  $k = k + 1$ ;
- 6:   Check the convergence conditions  $\|\mathcal{X}^{k+1} - \mathcal{X}^k\|_\infty \leq \epsilon$ .
- 7: **end while**
- 8: **return**  $\mathcal{X}^{k+1}$ .

**Output:** Completed tensor  $\mathcal{X} = \mathcal{X}^{k+1}$ .

---

of the FFM, i.e., a logarithmic function is applied to each singular value. The effectiveness of this relaxation has been confirmed in previous research [22], [49], [50], [51], [52], and this can improve the accuracy of the method. Therefore, the non-convex relaxation form of FFM proposed by us is as follows:

$$S^*(\mathcal{X}) = \sum_{1 \leq k_1 \leq k_2 \leq N} \beta_{k_1 k_2} \text{Log}(\mathcal{X}_{(k_1 k_2)}), \quad (11)$$

where

$$\text{Log}(\mathcal{X}_{(k_1 k_2)}) = \sum_m (\log(\sigma_m(\mathcal{X}_{(k_1)}) + \varepsilon)), \quad k_1 = k_2,$$

$$\text{Log}(\mathcal{X}_{(k_1 k_2)}) = \sum_{i=1}^{J_{k_1 k_2}} \sum_m (\log(\sigma_m(\mathcal{X}_{(k_1 k_2)}^{(i)}) + \varepsilon)), \quad k_1 \neq k_2,$$

are both with log-sum forms,  $\varepsilon$  is a small positive number, and  $\sigma_m(\mathcal{X}_{(k_1)})$  and  $\sigma_m(\mathcal{X}_{(k_1 k_2)}^{(i)})$  respectively defines the  $m$ -th singular value of  $\mathcal{X}_{(k_1)}$  and  $\mathcal{X}_{(k_1 k_2)}^{(i)}$ , and  $J_{k_1 k_2} = \prod_{s \neq k_1, k_2} I_s$ . In the later section, we will use this relaxation form of FFM to establish FFM-based models.

## 5 FFM-BASED MODELS AND SOLVING ALGORITHMS

In this section, we apply the FFM to low rank tensor complete (LRTC) and tensor robust principal component analysis (TRPCA) and propose the FFM-based models with ADMM-based solving algorithms.

### 5.1 FFM-based LRTC model

Tensor completion aims at estimating the missing elements from an incomplete observation tensor. Considering an  $N$ -order tensor  $\mathcal{X} \in \mathbb{R}^{I_1 \times I_2 \times \dots \times I_N}$ , the proposed FFM-based LRTC model is formulated as follow

$$\min_{\mathcal{X}} S^*(\mathcal{X}) \quad s.t. \quad \mathcal{P}_\Omega(\mathcal{X} - \mathcal{Z}) = 0, \quad (12)$$

where  $\mathcal{X}$  is the reconstructed tensor and  $\mathcal{Z}$  is the observed tensor,  $\Omega$  is the index set for the known entries, and  $\mathcal{P}_\Omega(\mathcal{X})$  is a projection operator that keeps the entries of  $\mathcal{X}$  in  $\Omega$  and sets all others to zero. Let

$$\Phi_{\mathbb{G}}(\mathcal{X}) := \begin{cases} 0, & \text{if } \mathcal{X} \in \mathbb{G}, \\ \infty, & \text{otherwise} \end{cases} \quad (13)$$

where  $\mathbb{G} := \{\mathcal{X} \in \mathbb{R}^{I_1 \times I_2 \times \dots \times I_N}, \mathcal{P}_\Omega(\mathcal{X} - \mathcal{Z}) = 0\}$ . Then (12) can be expressed equivalently as

$$\min_{\mathcal{X}} \sum_{1 \leq k_1 \leq k_2 \leq N} \beta_{k_1 k_2} \text{Log}(\mathcal{X}_{(k_1 k_2)}) + \Phi_{\mathbb{G}}(\mathcal{X}) \quad (14)$$

where  $\beta_{k_1 k_2} \geq 0$  ( $1 \leq k_1 \leq k_2 \leq N, k_1, k_2 \in \mathbb{Z}$ ) and  $\sum_{1 \leq k_1 \leq k_2 \leq N} \beta_{k_1 k_2} = 1$ . Next, we use the ADMM to solve (14). We first introduce auxiliary variables  $\mathcal{M}_{k_1 k_2}$ , and then rewrite (14) as the following equivalent constrained problem:

$$\min_{\mathcal{X}} \sum_{1 \leq k_1 \leq k_2 \leq N} \beta_{k_1 k_2} \text{Log}((\mathcal{M}_{k_1 k_2})_{(k_1 k_2)}) + \Phi_{\mathbb{G}}(\mathcal{X}) \quad (15)$$

*s.t.*  $\mathcal{X} = \mathcal{M}_{k_1 k_2}, 1 \leq k_1 \leq k_2 \leq N, k_1, k_2 \in \mathbb{Z}$ .

The augmented Lagrangian function of (15) can be expressed in the following concise form:

$$L_{\mu_{k_1 k_2}}(\mathcal{X}, \mathcal{M}_{k_1 k_2}, \mathcal{Q}_{k_1 k_2}) = \sum_{1 \leq k_1 \leq k_2 \leq N} \beta_{k_1 k_2} \text{Log}((\mathcal{M}_{k_1 k_2})_{(k_1 k_2)}) + \Phi_{\mathbb{G}}(\mathcal{X}) + \frac{\mu_{k_1 k_2}}{2} \|\mathcal{X} - \mathcal{M}_{k_1 k_2} + \frac{\mathcal{Q}_{k_1 k_2}}{\mu_{k_1 k_2}}\|_F^2, \quad (16)$$

where  $\mathcal{Q}_{k_1 k_2}$  ( $1 \leq k_1 \leq k_2 \leq N$ ) are the Lagrange multipliers,  $\mu_{k_1 k_2}$  are positive scalars. Then we can solve the problem under the ADMM framework. For the sake of convenience, we denote the variable updated by the iteration as  $(\cdot)^+$ , and omit the specific number of iterations.

Fixed  $\mathcal{X}$  and  $\mathcal{Q}_{k_1 k_2}$ , then  $\mathcal{M}_{k_1 k_2}$  can be solved by the following minimization problem:

$$\min_{\mathcal{M}_{k_1 k_2}} \sum_{1 \leq k_1 \leq k_2 \leq N} \beta_{k_1 k_2} \text{Log}((\mathcal{M}_{k_1 k_2})_{(k_1 k_2)}) + \frac{\mu_{k_1 k_2}}{2} \|\mathcal{X} - \mathcal{M}_{k_1 k_2} + \frac{\mathcal{Q}_{k_1 k_2}}{\mu_{k_1 k_2}}\|_F^2. \quad (17)$$

Since the relationship between  $k_1$  and  $k_2$  will produce different minimization problems, we divide (17) into two cases to consider.

In case 1:  $k_1 = k_2$ ,  $(\mathcal{M}_{k_1 k_2})_{(k_1 k_2)}$  is a matrix. In this case the problem (17) can be obtained as follows:

$$\min_{\mathcal{M}_{k_1 k_2}} \sum_{1 \leq k_1 \leq k_2 \leq N} \beta_{k_1 k_2} \sum_m (\log(\sigma_m(\mathcal{M}_{k_1 k_2})_{(k_1 k_2)} + \varepsilon)) + \frac{\mu_{k_1 k_2}}{2} \|\mathcal{X} - \mathcal{M}_{k_1 k_2} + \frac{\mathcal{Q}_{k_1 k_2}}{\mu_{k_1 k_2}}\|_F^2. \quad (18)$$

To solve (18), we introduce the following theorem [48].

**Theorem 2 ([48]).** Assuming that  $Y \in \mathbb{R}^{I_1 \times I_2}$  is a matrix, a minimizer to

$$\min_{\mathcal{X}} \alpha \text{Log}(\mathcal{X}) + \frac{1}{2} \|\mathcal{X} - Y\|_F^2,$$

is given by

$$\mathcal{X} = U \Sigma_\alpha V^T,$$

where  $\Sigma_\alpha = \text{diag}(D_{\alpha, \varepsilon}(\sigma_1), D_{\alpha, \varepsilon}(\sigma_2), \dots, D_{\alpha, \varepsilon}(\sigma_m))$  and  $Y = U \text{diag}(\sigma_1, \sigma_2, \dots, \sigma_m) V^T$ . Here,  $D_{\alpha, \varepsilon}(\cdot)$  is the thresholding operator defined as:

$$D_{\alpha, \varepsilon}(x) = \begin{cases} 0, & \text{if } |x| \leq 2\sqrt{\alpha} - \varepsilon, \\ \text{sign}(x) \left( \frac{l_1(x) + l_2(x)}{2} \right), & \text{if } |x| > 2\sqrt{\alpha} - \varepsilon \end{cases} \quad (19)$$

where  $l_1(x) = |x| - \varepsilon$ ,  $l_2(x) = \sqrt{(|x| + \varepsilon)^2 - 4\alpha}$ .

From Theorem 2, the update of  $\mathcal{M}_{k_1 k_2}$  can be obtained as follows:

$$\mathcal{M}_{k_1 k_2}^+ = \text{fold}_{k_1}(U_1 \Sigma_{\beta_{k_1 k_2}} V_1^T), \quad (20)$$

where  $U_1 \text{diag}(\sigma_1, \sigma_2, \dots, \sigma_m) V_1^T$  is the SVD of  $\text{unfold}_{k_1}(\mathcal{X} + \frac{\mathcal{Q}_{k_1 k_2}}{\mu_{k_1 k_2}})$ , and let  $\nu_{k_1 k_2} = \frac{\beta_{k_1 k_2}}{\mu_{k_1 k_2}}$ , then  $\Sigma_{\nu_{k_1 k_2}} = \text{diag}(D_{\nu_{k_1 k_2}, \varepsilon}(\sigma_1), D_{\nu_{k_1 k_2}, \varepsilon}(\sigma_2), \dots, D_{\nu_{k_1 k_2}, \varepsilon}(\sigma_m))$ .

In case 2:  $k_1 \neq k_2$ ,  $(\mathcal{M}_{k_1 k_2})_{(k_1 k_2)}$  is a three-order tensor. We transformed the question (17) into the following form:

$$\min_{\mathcal{M}_{k_1 k_2}} \sum_{1 \leq k_1 \leq k_2 \leq N} \beta_{k_1 k_2} \sum_{i=1}^{j_{k_1 k_2}} \sum_m (\log(\sigma_m(\mathcal{X}_{(k_1 k_2)}^{(i)})) + \varepsilon) + \frac{\mu_{k_1 k_2}}{2} \|\mathcal{X} - \mathcal{M}_{k_1 k_2} + \frac{\mathcal{Q}_{k_1 k_2}}{\mu_{k_1 k_2}}\|_F^2. \quad (21)$$

To solve (21), we introduce the following theorem [53].

**Theorem 3 ([53]).** For any  $\mathcal{A} \in \mathbb{R}^{I_1 \times I_2 \times I_3}$  and  $\lambda > 0$ , the local optimal solution of the following minimization

$$\min_{\mathcal{B}} \frac{1}{2} \|\mathcal{B} - \mathcal{A}\|_F^2 + \lambda \text{Log}(\mathcal{X}) \quad (22)$$

is given by  $\mathcal{B} = \mathcal{U} * \mathcal{S}_1 * \mathcal{V}^H$ , where  $\mathcal{U}$  and  $\mathcal{V}$  derive from the t-SVD of  $\mathcal{A} = \mathcal{U} * \mathcal{S}_2 * \mathcal{V}^H$ . More importantly, the  $i$ th frontal slice of DFT of  $\mathcal{S}_1$  and  $\mathcal{S}_2$ , i.e.,  $\bar{\mathcal{S}}_1^{(i)} = \text{diag}(\sigma_1(\bar{\mathcal{B}}^{(i)}), \sigma_2(\bar{\mathcal{B}}^{(i)}), \dots, \sigma_m(\bar{\mathcal{B}}^{(i)}))$  and  $\bar{\mathcal{S}}_2^{(i)} = \text{diag}(\sigma_1(\bar{\mathcal{A}}^{(i)}), \sigma_2(\bar{\mathcal{A}}^{(i)}), \dots, \sigma_m(\bar{\mathcal{A}}^{(i)}))$ , has the following relationship

$$\sigma_j(\bar{\mathcal{B}}^{(i)}) = \begin{cases} \frac{1}{2}(\sqrt{\Delta_{ij}} + \sigma_j(\bar{\mathcal{A}}^{(i)}) - \varepsilon), & \text{if } \Delta_{ij} > 0, \\ \sqrt{\Delta_{ij}} > \varepsilon - \sigma_j(\bar{\mathcal{A}}^{(i)}), & \sigma_j^2(\bar{\mathcal{A}}^{(i)}) > 2\phi; \\ 0, & \text{otherwise.} \end{cases} \quad (23)$$

where

$$\Delta_{ij} = (\sigma_j(\bar{\mathcal{A}}^{(i)}) + \varepsilon)^2 - 4\lambda, \\ \phi = \frac{1}{8}(\sqrt{\Delta_{ij}} - \sigma_j(\bar{\mathcal{A}}^{(i)}) - \varepsilon)^2 + \lambda \log\left(\frac{\sigma_j(\bar{\mathcal{A}}^{(i)}) + \sqrt{\Delta_{ij}} + \varepsilon}{2\varepsilon}\right).$$

From Theorem 3, the update of  $\mathcal{M}_{k_1 k_2}$  can be obtained as follows:

$$\mathcal{M}_{k_1 k_2}^+ = t - \text{fold}(\mathcal{U} * \mathcal{S}_1 * \mathcal{V}^H, k_1, k_2), \quad (24)$$

where  $\mathcal{S}_1$  is given by Theorem 3 and  $\mathcal{U} * \mathcal{S}_2 * \mathcal{V}^H$  is the t-SVD of  $t - \text{unfold}(\mathcal{X} + \frac{\mathcal{Q}_{k_1 k_2}}{\mu_{k_1 k_2}}, k_1, k_2)$ .

In summary, the update of  $\mathcal{M}_{k_1 k_2}$  is expressed in the following form:

$$\mathcal{M}_{k_1 k_2}^+ = \begin{cases} \text{fold}_{k_1}(U_1 \Sigma_{\beta_{k_1 k_2}} V_1^T), & \text{if } k_1 = k_2, \\ t - \text{fold}(\mathcal{U} * \mathcal{S}_1 * \mathcal{V}^H, k_1, k_2), & \text{if } k_1 \neq k_2 \end{cases} \quad (25)$$

Fixed  $\mathcal{M}_{k_1 k_2}$  and  $\mathcal{Q}_{k_1 k_2}$ , the minimization problem of  $\mathcal{X}$  is as follows:

$$\min_{\mathcal{X}} \Phi_{\mathbb{G}}(\mathcal{X}) + \sum_{1 \leq k_1 \leq k_2 \leq N} \frac{\mu_{k_1 k_2}}{2} \|\mathcal{X} - \mathcal{M}_{k_1 k_2} + \frac{\mathcal{Q}_{k_1 k_2}}{\mu_{k_1 k_2}}\|_F^2. \quad (26)$$

The closed form of  $\mathcal{X}$  can be derived by setting the derivative of (26) to zero. We can now update  $\mathcal{X}$  by the following equation:

$$\mathcal{X}^+ = \mathcal{P}_{\Omega^c} \left( \frac{\sum_{1 \leq k_1 \leq k_2 \leq N} \mu_{k_1 k_2} (\mathcal{M}_{k_1 k_2} - \frac{\mathcal{Q}_{k_1 k_2}}{\mu_{k_1 k_2}})}{\sum_{1 \leq k_1 \leq k_2 \leq N} \mu_{k_1 k_2}} \right) + \mathcal{P}_{\Omega}(\mathcal{Z}) \quad (27)$$

### Algorithm 3 FFMTPRCA

**Input:** The corrupted observation tensor  $\mathcal{T}$ , convergence criteria  $\epsilon$ , maximum iteration number  $K$ .

**Initialization:**  $\mathcal{L}^0 = \mathcal{T}$ ,  $\mathcal{G}_{l_1 l_2}^0 = \mathcal{L}^0$ ,  $\mu_{l_1 l_2}^0 > 0$ ,  $\rho > 0$ ,  $\tau > 1$ .

- 1: **while** not converged and  $k < K$  **do**
- 2: Updating  $\mathcal{G}_{l_1 l_2}^k$  via (33);
- 3: Updating  $\mathcal{L}^k$  via (35);
- 4: Updating  $\mathcal{E}^k$  via (37);
- 5: Updating the multipliers  $\mathcal{R}_{k_1 k_2}^k$  and  $\mathcal{F}^k$  via (39);
- 6:  $\mu_{k_1 k_2}^k = \tau \mu_{k_1 k_2}^{k-1}$ ,  $\rho^k = \tau \rho^{k-1}$   $k = k + 1$ ;
- 7: Check the convergence conditions  $\|\mathcal{L}^{k+1} - \mathcal{L}^k\|_{\infty} \leq \epsilon$ .
- 8: **end while**
- 9: **return**  $\mathcal{L}^{k+1}$  and  $\mathcal{E}^{k+1}$ .

**Output:**  $\mathcal{L}$  and  $\mathcal{E}$ .

Finally, multipliers  $\mathcal{Q}_{k_1 k_2}$  are updated as follows:

$$\mathcal{Q}_{k_1 k_2}^+ = \mathcal{Q}_{k_1 k_2} + \mu_{k_1 k_2} (\mathcal{X} - \mathcal{M}_{k_1 k_2}). \quad (28)$$

FFM-based LRTC model computation is given in Algorithm 2. The main per-iteration cost lies in the update of  $\mathcal{M}_{k_1 k_2}$ , which requires computing SVD and t-SVD. The per-iteration complexity is  $O(LE(\sum_{1 \leq k_1 < k_2 \leq N} [\log(l_{e_{k_1 k_2}}) + \min(I_{k_1}, I_{k_2})] + \sum_{1 \leq k_1 \leq N} I_{k_1}))$ , where  $LE = \prod_{i=1}^N I_i$  and  $l_{e_{k_1 k_2}} = LE / (I_{k_1} I_{k_2})$ .

## 5.2 FFM-based TRPCA model

Tensor robust PCA (TRPCA) aims to recover the tensor from grossly corrupted observations. Using the proposed FFM, we can get the following FFM-based TRPCA model:

$$\min_{\mathcal{L}, \mathcal{E}} S^*(\mathcal{L}) + \tau \|\mathcal{E}\|_1 \quad \text{s.t.} \quad \mathcal{T} = \mathcal{L} + \mathcal{E}, \quad (29)$$

where  $\mathcal{T}$  is the corrupted observation tensor,  $\mathcal{L}$  is the low-rank component,  $\mathcal{E}$  is the sparse component, and  $\tau$  is a tuning parameter compromising  $\mathcal{L}$  and  $\mathcal{E}$ . We use the ADMM to solve (29). Firstly, we introduce auxiliary variables  $\mathcal{G}_{l_1 l_2}$ , and then rewrite (29) as the following equivalent constrained problem:

$$\min_{\mathcal{L}, \mathcal{E}} \sum_{1 \leq l_1 \leq l_2 \leq N} \beta_{l_1 l_2} \text{Log}((\mathcal{G}_{l_1 l_2})_{(l_1 l_2)}) + \tau \|\mathcal{E}\|_1 \\ \text{s.t.} \quad \mathcal{T} = \mathcal{L} + \mathcal{E}, \\ \mathcal{L} = \mathcal{G}_{l_1 l_2}, 1 \leq l_1 \leq l_2 \leq N, l_1, l_2 \in \mathbb{Z}. \quad (30)$$

The augmented Lagrangian function of (30) can be expressed in the following concise form:

$$L_{\mu_{l_1 l_2}, \rho}(\mathcal{L}, \mathcal{G}_{l_1 l_2}, \mathcal{E}, \mathcal{R}_{k_1 k_2}, \mathcal{F}) = \tau \|\mathcal{E}\|_1 \\ + \sum_{1 \leq l_1 \leq l_2 \leq N} \beta_{l_1 l_2} \text{Log}((\mathcal{G}_{l_1 l_2})_{(l_1 l_2)}) \\ + \frac{\mu_{l_1 l_2}}{2} \|\mathcal{L} - \mathcal{G}_{l_1 l_2} + \frac{\mathcal{R}_{l_1 l_2}}{\mu_{l_1 l_2}}\|_F^2 + \frac{\rho}{2} \|\mathcal{T} - \mathcal{L} - \mathcal{E} + \frac{\mathcal{F}}{\rho}\|_F^2. \quad (31)$$

where  $\mathcal{F}$  and  $R_{l_1 l_2}$  ( $1 \leq k_1 \leq k_2 \leq N$ ) are the Lagrange multipliers,  $\mu_{k_1 k_2}$  and  $\rho$  are positive scalar. Then we can solve the problem under the ADMM framework. Similar to FFM-based LRTC model, we denote the variable updated by the iteration as  $(\cdot)^+$ , and omit the specific number of iterations.

Fixed  $\mathcal{L}$ ,  $\mathcal{E}$ ,  $\mathcal{R}_{k_1 k_2}$  and  $\mathcal{F}$ , then  $\mathcal{G}_{l_1 l_2}$  can be solved by the following minimization problem:

$$\min_{\mathcal{G}_{l_1 l_2}} \sum_{1 \leq l_1 \leq l_2 \leq N} \beta_{l_1 l_2} \text{Log}((\mathcal{G}_{l_1 l_2})_{(l_1 l_2)}) + \frac{\mu_{l_1 l_2}}{2} \|\mathcal{L} - \mathcal{G}_{l_1 l_2} + \frac{\mathcal{R}_{l_1 l_2}}{\mu_{l_1 l_2}}\|_{\mathcal{F}}^2 \quad (32)$$

From the solution process of  $M_{k_1 k_2}$  in FFM-based LRTC model, the update of  $\mathcal{G}_{l_1 l_2}$  is as follows:

$$\mathcal{G}_{l_1 l_2}^+ = \begin{cases} \text{fold}_{l_1}(U_1 \Sigma^{\beta_{l_1 l_2}} V_1^T), & \text{if } l_1 = l_2, \\ t - \text{fold}(\mathcal{U} * \mathcal{S}_1 * \mathcal{V}^H, l_1, l_2), & \text{if } l_1 \neq l_2 \end{cases} \quad (33)$$

where  $U_1 \text{diag}(\sigma_1, \sigma_2, \dots, \sigma_m) V_1^T$  is the SVD of  $\text{unfold}_{l_1}(\mathcal{L} + \frac{\mathcal{R}_{l_1 l_2}}{\mu_{l_1 l_2}})$  and  $\mathcal{S}_1$  is given by Theorem 3 and  $\mathcal{U} * \mathcal{S}_2 * \mathcal{V}^H$  is the t-SVD of  $t - \text{unfold}(\mathcal{L} + \frac{\mathcal{R}_{l_1 l_2}}{\mu_{l_1 l_2}}, l_1, l_2)$ .

Then fixed  $\mathcal{G}_{l_1 l_2}$ ,  $\mathcal{E}$ ,  $\mathcal{R}_{k_1 k_2}$  and  $\mathcal{F}$ , the minimization problem  $\mathcal{L}$  is converted into the following form:

$$\min_{\mathcal{L}} \sum_{1 \leq l_1 \leq l_2 \leq N} \beta_{l_1 l_2} \frac{\mu_{l_1 l_2}}{2} \|\mathcal{L} - \mathcal{G}_{l_1 l_2} + \frac{\mathcal{R}_{l_1 l_2}}{\mu_{l_1 l_2}}\|_{\mathcal{F}}^2 + \frac{\rho}{2} \|\mathcal{T} - \mathcal{L} - \mathcal{E} + \frac{\mathcal{F}}{\rho}\|_{\mathcal{F}}^2. \quad (34)$$

The closed form of  $\mathcal{L}$  can be derived by setting the derivative of (34) to zero. We can now update  $\mathcal{L}$  by the following equation:

$$\mathcal{L}^+ = \frac{\sum_{1 \leq l_1 \leq l_2 \leq N} \mu_{l_1 l_2} (\mathcal{G}_{l_1 l_2} - \frac{\mathcal{R}_{l_1 l_2}}{\mu_{l_1 l_2}}) + \rho(\mathcal{T} - \mathcal{E} + \frac{\mathcal{F}}{\rho})}{\sum_{1 \leq l_1 \leq l_2 \leq N} \mu_{l_1 l_2} + \rho}. \quad (35)$$

Now, let's solve  $\mathcal{E}$ . The minimization problem of  $\mathcal{E}$  is as follows:

$$\min_{\mathcal{E}} \tau \|\mathcal{E}\|_1 + \frac{\rho}{2} \|\mathcal{T} - \mathcal{L} - \mathcal{E} + \frac{\mathcal{F}}{\rho}\|_{\mathcal{F}}^2. \quad (36)$$

Problem (36) has the following closed-form solution:

$$\mathcal{E}^+ = S_{\tau}(\mathcal{T} - \mathcal{L} + \frac{\mathcal{F}}{\rho}), \quad (37)$$

where  $S_{\lambda}(\cdot)$  is the soft thresholding operator [54]:

$$S_{\lambda}(x) = \begin{cases} 0, & \text{if } |x| \leq \lambda, \\ \text{sign}(x)(|x| - \lambda), & \text{if } |x| > \lambda \end{cases} \quad (38)$$

Finally, multipliers  $\mathcal{R}_{l_1 l_2}$  and  $\mathcal{F}$  are updated according to the following formula:

$$\begin{cases} \mathcal{R}_{l_1 l_2}^+ = \mathcal{R}_{k_1 k_2} + \mu_{l_1 l_2} (\mathcal{L} - \mathcal{G}_{l_1 l_2}); \\ \mathcal{F}^+ = \mathcal{F} + \rho(\mathcal{T} - \mathcal{L} - \mathcal{E}). \end{cases} \quad (39)$$

FFM-based TPRCA model computation is given in Algorithm 3. The main per-iteration cost lies in the update of  $\mathcal{G}_{l_1 l_2}$ , which requires computing SVD and t-SVD. The per-iteration complexity is  $O(LE(\sum_{1 \leq l_1 < l_2 \leq N} [\log(l_{l_1 l_2}) + \min(l_1, l_2)] + \sum_{1 \leq l_1 \leq N} l_1))$ , where  $LE = \prod_{i=1}^N l_i$  and  $l_{l_1 l_2} = LE / (l_1 l_2)$ .

TABLE 1

The names and corresponding labels of individual MSI in the database CAVE.

ID	MSI name	ID	MSI name
1	watercolors	17	fake_and_real_tomatoes
2	thread_spools	18	fake_and_real_sushi
3	superballs	19	fake_and_real_strawberries
4	stuffed_toys	20	fake_and_real_peppers
5	sponges	21	fake_and_real_lemons
6	real_and_fake_peppers	22	fake_and_real_lemon_slices
7	real_and_fake_apples	23	fake_and_real_food
8	pompoms	24	fake_and_real_beers
9	photo_and_face	25	face
10	paints	26	egyptian_statue
11	oil_painting	27	cloth
12	jelly_beans	28	clay
13	hairs	29	chart_and_stuffed_toy
14	glass_tiles	30	beads
15	flowers	31	balloons
16	feathers	32	cd

## 6 NUMERICAL EXPERIMENTS

We evaluate the performance of the proposed FFM-based LRTC and TRPCA methods. All methods are tested on real-world data. We employ the peak signal-to-noise rate (PSNR), the structural similarity (SSIM) [55], the feature similarity (FSIM) [56], and erreur relative globale adimensionnelle de synthèse (ERGAS) [57] to measure the quality of the recovered results. The higher the value of PSNR, SSIM and FSIM is, the better the quality of the recovered image will be. Meanwhile, the smaller the ERGAS value is, the better the quality of the recovered image will be. All tests are implemented on the Windows 10 platform and MATLAB (R2019a) with an Intel Core i7-10875H 2.30 GHz and 32 GB of RAM.

### 6.1 Low-rank tensor completion

In this section, we test four kinds of real-world data: MSI, MRI, color video (CV), and hyperspectral video (HSV). The methodology for sampling the data is purely random sampling. The compared LRTC methods are as follows: HaLRTC [43], LRTCTV-I [58], KBRTC [48] and ESPTC [4], representing state-of-the-art for the Tucker-decomposition-based method; and TNN [59], PSTNN [60], FTNN [61], WSTNN [38], nonconvex WSTNN [62], representing state-of-the-art for the t-SVD-based method; and minmax concave plus penalty-based TC method (McpTC) [63] and a novel low-rank tensor completion model using smooth matrix factorization (SMFLRTC)[64]. In view of the fact that the four of them, i.e., the TNN, the PSTNN, the FTNN, and the SMFLRTC apply only to three-order tensors, in all four-order tensor tests, we first reshape the four-order tensors into three-order tensors and then test the performances of these methods.

#### 6.1.1 MSI completion

We test 32 MSIs in the dataset CAVE<sup>1</sup>. All testing data are of size  $256 \times 256 \times 31$ . First, we label 32 MSI in the database, and their detailed names and corresponding numbers are listed in Table 1. Then, we randomly select 9 of the 32

1. <http://www.cs.columbia.edu/CAVE/databases/multispectral/>

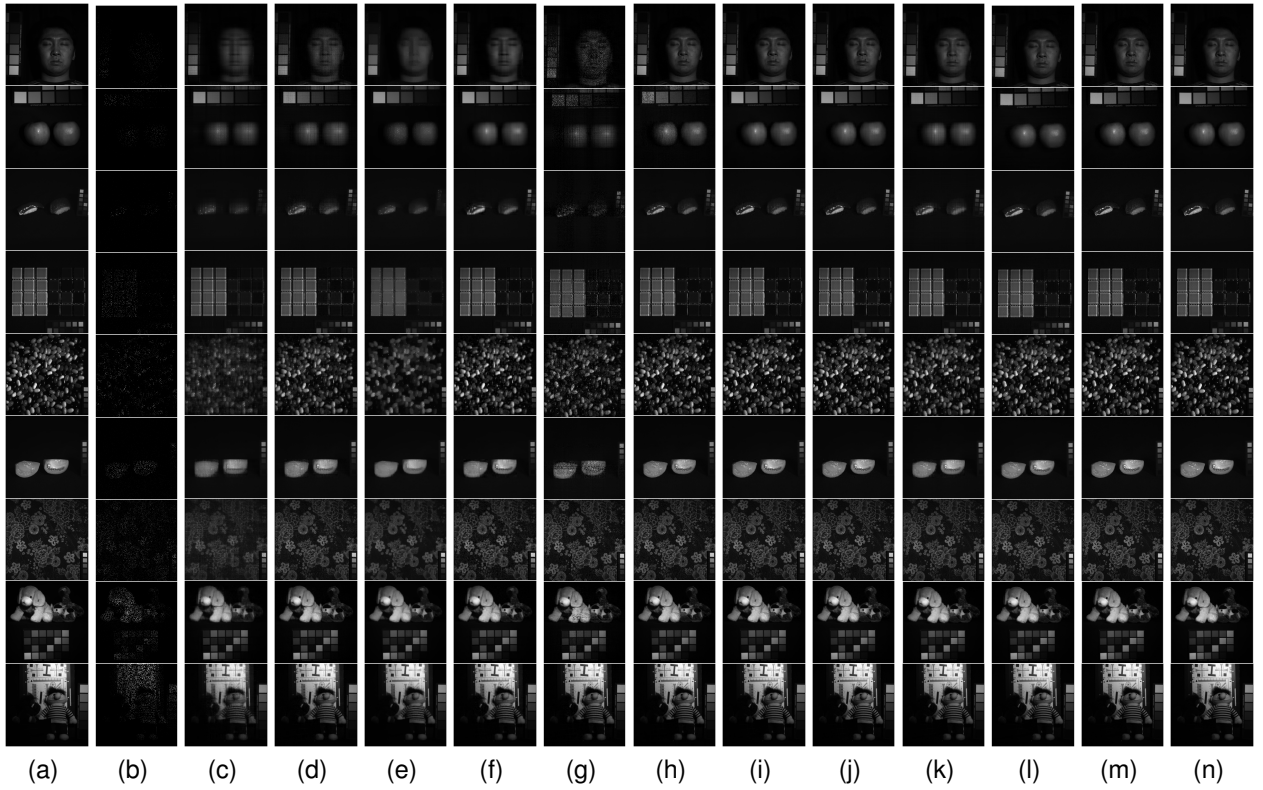


Fig. 2. (a) Original image. (b) Observed image. (c) HaLRTC. (d) TNN. (e) LRTCCTV-I. (f) McpTC. (g) PSTNN. (h) SMFLRTC. (i) KBRTC. (j) ESPTC. (k) FTNN. (l) WSTNN. (m) NWSTNN. (n) FFMTC. SR: top 3 rows is 5%, middle 3 rows is 10% and last 3 rows is 20%. The rows of MSIs are in order: face, real\_and\_fake\_apples, fake\_and\_real\_sushi, glass\_tiles, jelly\_beans, fake\_and\_real\_tomatoes, cloth, stuffed\_toys, chart\_and\_stuffed\_toy. The corresponding bands in each row are: 10, 30, 20, 8, 18, 28, 5, 15, 25.

TABLE 2  
The average PSNR, SSIM, FSIM and ERGAS values for 32 MSIs tested by observed and the twelve utilized LRTC methods.

SR Method	5%				10%				20%				Time(s)
	PSNR	SSIM	FSIM	ERGAS	PSNR	SSIM	FSIM	ERGAS	PSNR	SSIM	FSIM	ERGAS	
Observed	15.438	0.153	0.644	845.374	15.672	0.194	0.646	822.902	16.185	0.269	0.651	775.704	0.000
HaLRTC	25.347	0.774	0.837	299.279	29.821	0.856	0.894	185.726	35.048	0.930	0.947	105.188	10.223
TNN	25.328	0.713	0.817	290.398	33.095	0.879	0.918	128.242	40.229	0.964	0.972	58.755	30.425
LRTCCTV-I	25.867	0.800	0.835	277.506	30.699	0.890	0.906	163.071	35.542	0.949	0.957	94.078	180.325
McpTC	32.476	0.875	0.909	133.036	35.974	0.925	0.943	91.923	40.522	0.964	0.971	56.109	186.442
PSTNN	18.710	0.474	0.650	575.015	23.186	0.682	0.782	353.671	34.388	0.924	0.941	115.934	32.702
SMFLRTC	31.503	0.887	0.918	146.535	39.284	0.964	0.972	60.816	44.031	0.980	0.985	37.596	533.010
KBRTC	36.261	0.930	0.948	88.631	42.638	0.977	0.982	42.779	48.639	0.993	0.995	21.691	113.016
ESPTC	36.170	0.925	0.946	90.600	41.763	0.971	0.977	47.085	47.249	0.989	0.992	25.717	190.471
FTNN	32.583	0.898	0.923	132.496	37.187	0.954	0.963	78.753	43.080	0.984	0.987	41.455	183.045
WSTNN	34.796	0.947	0.952	96.183	40.120	0.981	0.981	53.209	47.124	0.995	0.995	24.774	48.983
NWSTNN	37.395	0.945	0.950	71.581	43.711	0.985	0.985	35.748	51.369	0.997	0.997	15.519	85.176
FFMTC	<b>40.350</b>	<b>0.971</b>	<b>0.976</b>	<b>54.134</b>	<b>45.860</b>	<b>0.990</b>	<b>0.991</b>	<b>29.272</b>	<b>52.386</b>	<b>0.998</b>	<b>0.998</b>	<b>13.990</b>	<b>107.509</b>

MSI and show their visual results at different sampling rates and different bands in Fig.2. The names of the individual MSI and their corresponding bands are reported in the caption of Fig.2. As can be seen from the Fig.2, our method is significantly superior to other methods in terms of visual results of different MSI at different sampling rates. It is especially worth mentioning that our method can still achieve excellent results even at a low sampling rate. To further highlight the superiority of our method, we list the average quantitative results of 32 MSIs in Table 2. It is not difficult to find that the PSNR value of our method at any sampling rate is at least 1db higher than that of the

suboptimal method. In particular, the PSNR value obtained by our method at 5% sampling rate is 3db higher than that of the suboptimal method, and the numerical results of SSIM, FSIM, and ERGAS are significantly better than other state-of-the-art methods. Finally, the PSNR, SSIM and FSIM values of 32 MSI obtained by different restoration methods are presented in the form of bar charts in Fig.3. It can be seen that our method performs extremely well for each MSI. But the suboptimal method is not always the NWSTNN method in Table 2. For example, for some MSI, the KBRTC method is superior to the NWSTNN method. In summary, it can be concluded that our method is superior to other state-of-the-

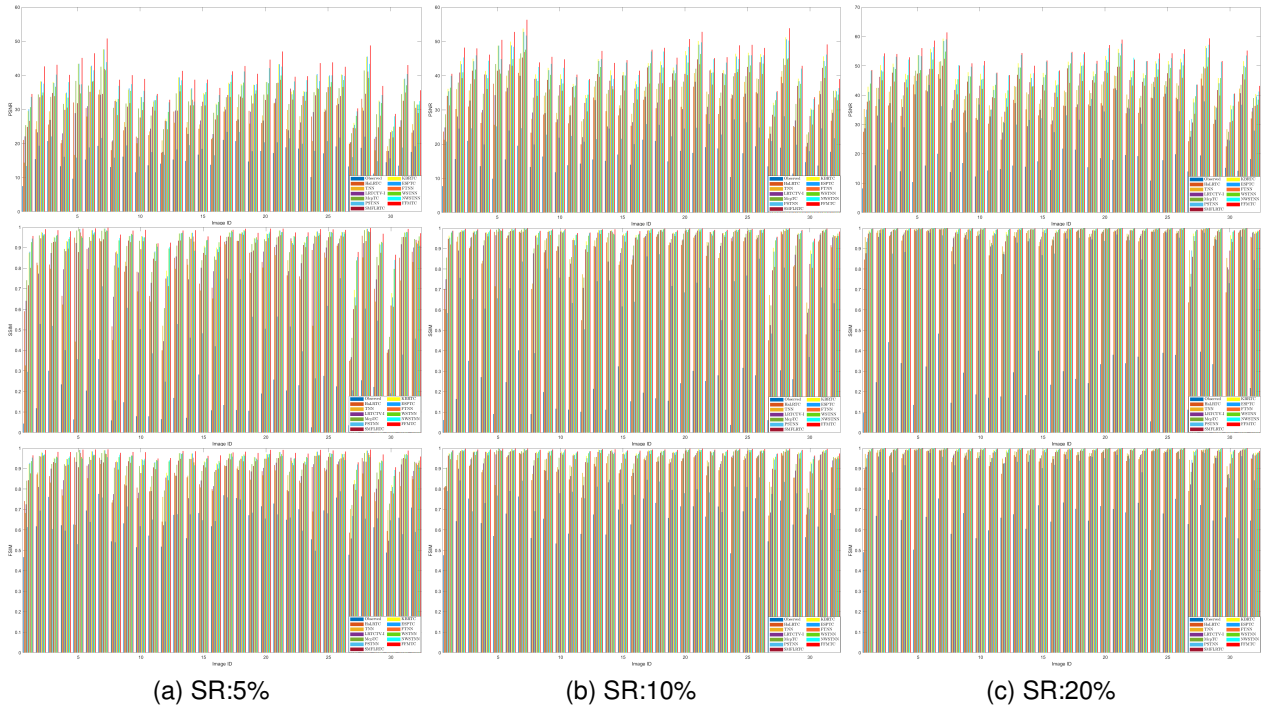


Fig. 3. Comparison of the PSNR values (top), SSIM values (middle) and FSIM values (bottom) obtained by FFMTC and the state-of-the-art methods on 32 MSIs. SR: (a)5%, (b)10%, (c)20%.

art methods in MSI experiments.

### 6.1.2 MRI completion

We test the performance of the proposed method and the comparison method on MRI<sup>2</sup> data with the size of  $181 \times 217 \times 181$ . Firstly, the visual results of MRI slices in different directions are shown in Fig.4, in which slice results of the same rank are used for the same sampling rate. Through observation, we see that the results restored by the suboptimal method, i.e., the NWSTNN method, still have certain ambiguity, while the results obtained by our method do not have this defect, and the most outstanding is that the results in all directions are the best. Therefore, we conclude that our method shows excellent comprehensiveness in the measure of tensor sparse features. Then, we list in Table 3 the average quantitative results of frontal slices recovered by all methods of MRI at different sampling rates. Obviously, the PSNR value of our method is at least 0.5dB higher than that of the suboptimal method, and the numerical results of SSIM, FSIM and ERGAS are obviously better than that of the suboptimal method. Therefore, the proposed method also has high efficiency in MRI data recovery.

### 6.1.3 CV completion

We test seven CVs<sup>3</sup>(respectively named news, akiyo, foreman, hall, highway, container, coastguard) of size  $144 \times 176 \times 3 \times 50$ . Firstly, we report the visual results of 7 CVs in our experiment in Fig.5, in which the frame number and sampling rate corresponding to each CV are described in the annotation. Obviously, we can see from the figure that our

results are optimal. Furthermore, the average quantitative results of 7 CVs are listed in Table 4. By comparison, it is found that the value of PSNR of our method is at least 0.4 dB higher than that of the suboptimal method, and the PSNR result of our method is 1.2 dB higher than that of the suboptimal method at 5% sampling rate. Finally, the quantitative results of each CV are displayed in a bar chart in Fig.6. We clearly see that our method still maintains great advantages for CV experiments.

### 6.1.4 HSV completion

We test an HSV<sup>4</sup> of size  $120 \times 188 \times 33 \times 31$ . Specifically, this HSV has 31 frames, and each frame has 33 bands of wavelengths of from 400 nm to 720 nm with a 10 nm step [65]. In Fig.7, we show the results of different frame numbers and different bands with three sampling rates. Experimental results show that our method is significantly better than other methods in restoring texture information. Table 5 lists the values of the PSNR, SSIM, FSIM and ERGAS of the tested HSV recovered by different LRTC methods. The experimental results exhibit that the proposed method has reached the highest value in all evaluation indicators. No matter how the SR is set, compared with the sub-optimal method, the method achieves a gain of about 0.7dB in the PSNR.

## 6.2 Tensor robust principal component analysis

In this section, we evaluate the performance of the proposed FFM-based TRPCA method by HSI denoising. The compared TRPCA methods include the SNN [66], TNN [41], 3DTNN and 3DLogTNN [62].

2. [http://brainweb.bic.mni.mcgill.ca/brainweb/selection\\_normal.html](http://brainweb.bic.mni.mcgill.ca/brainweb/selection_normal.html)

3. <http://trace.eas.asu.edu/yuv/>

4. <http://openremotesensing.net/knowledgebase/hyperspectral-video/>.

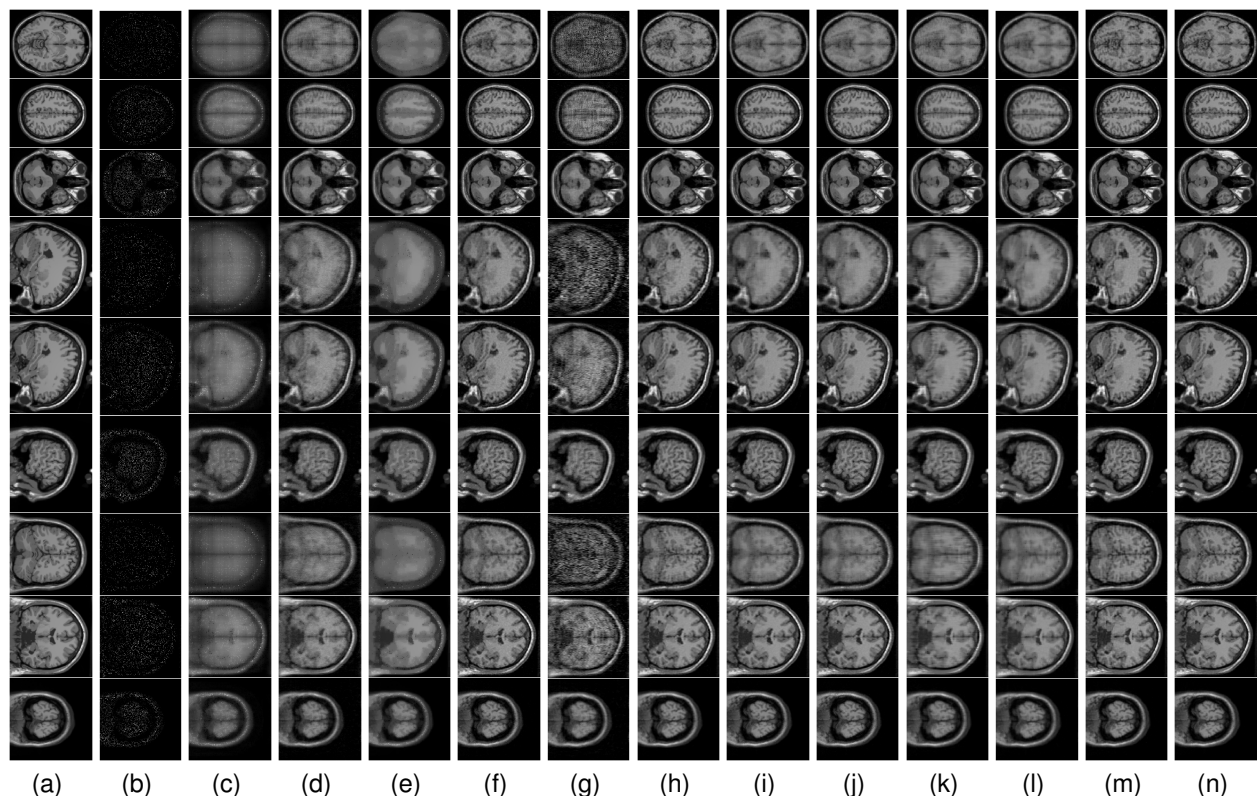


Fig. 4. (a) Original image. (b) Observed image. (c) HaLRTC. (d) TNN. (e) LRTCTV-I. (f) McpTC. (g) PSTNN. (h) SMFLRTC. (i) KBRTC. (j) ESPTC. (k) FTNN. (l) WSTNN. (m) NWSTNN. (n) FFMTC. Comparison of FFMTC and the state-of-the-art methods on the MRI of the Frontal slices (top 3 row), Horizontal slices (middle 3 row) and Lateral slices (bottom 3 row). Each type of slice: the first row is the 65th slice with a sampling rate of 5%, the second row is the 120th slice with a sampling rate of 10%, and the third row is the 33th slice with a sampling rate of 20%.

TABLE 3  
The PSNR, SSIM, FSIM and ERGAS values output by observed and the twelve utilized LRTC methods for MRI.

SR Method	5%				10%				20%				Time(s)
	PSNR	SSIM	FSIM	ERGAS	PSNR	SSIM	FSIM	ERGAS	PSNR	SSIM	FSIM	ERGAS	
Observed	11.399	0.310	0.530	1021.127	11.635	0.323	0.565	993.791	12.145	0.350	0.612	937.049	0.000
HaLRTC	17.291	0.298	0.638	537.831	20.131	0.439	0.726	389.565	24.426	0.659	0.829	235.793	27.316
TNN	22.725	0.471	0.743	302.480	26.079	0.642	0.812	205.024	29.973	0.799	0.882	130.965	97.054
LRTCTV-I	19.377	0.598	0.702	432.845	22.895	0.750	0.806	292.166	28.184	0.890	0.908	155.939	671.241
McpTC	27.939	0.749	0.843	153.404	31.459	0.845	0.888	102.679	35.569	0.937	0.941	63.986	622.650
PSTNN	16.196	0.197	0.589	606.927	22.447	0.438	0.723	307.792	29.577	0.767	0.870	137.637	113.446
SMFLRTC	28.527	0.792	0.859	146.250	32.187	0.895	0.911	95.272	35.119	0.944	0.943	66.885	1996.388
KBRTC	26.126	0.728	0.831	192.742	32.696	0.912	0.924	89.493	37.089	0.967	0.966	53.662	335.954
ESPTC	25.534	0.695	0.820	208.066	32.535	0.904	0.918	91.721	35.969	0.949	0.949	61.482	546.520
FTNN	24.884	0.693	0.836	231.625	28.348	0.826	0.895	151.686	32.738	0.923	0.945	89.804	1280.618
WSTNN	25.557	0.709	0.825	211.023	29.100	0.837	0.888	138.317	33.472	0.928	0.940	83.124	277.745
NWSTNN	30.221	0.826	0.883	120.052	33.294	0.902	0.924	83.646	36.849	0.950	0.956	55.015	458.180
FFMTC	<b>30.893</b>	<b>0.880</b>	<b>0.902</b>	<b>109.815</b>	<b>34.160</b>	<b>0.934</b>	<b>0.937</b>	<b>75.110</b>	<b>37.891</b>	<b>0.969</b>	<b>0.967</b>	<b>48.770</b>	<b>434.761</b>

### 6.2.1 HSI denoising

We test the Pavia University and Washington DC Mall and Houston HSI data sets, where Pavia data size is  $200 \times 200 \times 80$  and Washington DC Mall data size is  $256 \times 256 \times 150$  and Houston data size is  $256 \times 256 \times 100$ . The random salt-pepper noise level (NL) is set to 0.2 and 0.4. In Fig.8, we show 3-D visualization of the denoising results and one band in these three HSIs. The results demonstrate that among the five comparative methods, the FFM-based TRPCA method achieves the best visual effects in terms of denoising and detail protection. Table 6 lists the PSNR, SSIM, and FSIM values of three tested HSIs recovered by different methods.

It is not difficult to see that the PSNR of our method is at least 1dB higher than that of the suboptimal method in any case. In particular, when NL is 0.2, the SSIM and FSIM obtained by our method are almost perfect.

### 6.3 Convergency Behaviours

We take the completeness of MRI, CV, MSI data and the robust principal component analysis of HSI as examples to illustrate the convergence behavior of the algorithm under different sampling rates and different noise levels. We have drawn  $\|\mathcal{X}^{k+1} - \mathcal{X}^k\|_\infty$  and  $\|\mathcal{L}^{k+1} - \mathcal{L}^k\|_\infty$  for each iteration

TABLE 4  
The average PSNR, SSIM, FSIM and ERGAS values for 7 CVs tested by observed and the twelve utilized LRTC methods.

SR	5%				10%				20%				Time(s)
Method	PSNR	SSIM	FSIM	ERGAS	PSNR	SSIM	FSIM	ERGAS	PSNR	SSIM	FSIM	ERGAS	
Observed	5.793	0.011	0.420	1194.943	6.028	0.019	0.423	1163.006	6.538	0.034	0.429	1096.668	0.000
HaLRTC	17.339	0.488	0.696	329.274	21.134	0.622	0.774	214.716	24.964	0.772	0.862	137.902	15.661
TNN	27.043	0.772	0.886	113.373	30.464	0.855	0.928	79.447	33.661	0.909	0.955	56.828	43.497
LRTCTV-I	19.482	0.579	0.692	273.371	21.205	0.655	0.771	228.372	25.776	0.816	0.881	127.382	291.480
McpTC	23.363	0.660	0.816	168.038	28.081	0.814	0.898	97.166	30.878	0.881	0.934	70.218	313.965
PSTNN	16.152	0.313	0.665	364.861	27.901	0.777	0.890	102.994	33.223	0.906	0.952	59.007	44.006
SMFLRTC	26.099	0.777	0.873	119.374	31.967	0.906	0.949	62.964	35.497	0.946	0.971	42.931	856.302
KBRTC	22.103	0.545	0.774	190.439	24.117	0.646	0.824	150.466	27.734	0.787	0.893	99.394	158.768
ESPTC	20.498	0.461	0.736	228.808	21.391	0.519	0.763	206.860	24.087	0.645	0.827	151.579	305.808
FTNN	26.092	0.789	0.886	127.310	29.455	0.875	0.928	84.665	33.055	0.934	0.960	56.255	648.280
WSTNN	29.212	0.872	0.920	88.525	32.676	0.923	0.951	61.909	36.539	0.960	0.975	40.870	200.654
NWSTNN	30.382	0.850	0.932	80.843	34.511	0.916	0.961	52.606	39.120	0.963	0.982	31.234	319.875
FFMTC	<b>31.592</b>	<b>0.889</b>	<b>0.943</b>	<b>69.471</b>	<b>35.296</b>	<b>0.936</b>	<b>0.967</b>	<b>47.310</b>	<b>39.521</b>	<b>0.969</b>	<b>0.984</b>	<b>29.423</b>	<b>341.327</b>

TABLE 5  
The PSNR, SSIM, FSIM and ERGAS values output by observed and the twelve utilized LRTC methods for HSV.

SR	5%				10%				20%				Time(s)
Method	PSNR	SSIM	FSIM	ERGAS	PSNR	SSIM	FSIM	ERGAS	PSNR	SSIM	FSIM	ERGAS	
Observed	10.761	0.029	0.501	924.271	10.995	0.047	0.513	899.681	11.507	0.083	0.529	848.164	0.000
HaLRTC	18.213	0.479	0.710	409.377	21.565	0.629	0.803	280.265	28.091	0.845	0.913	134.492	119.097
TNN	26.632	0.821	0.909	154.287	36.716	0.957	0.976	49.763	41.185	0.981	0.989	29.945	284.852
LRTCTV-I	21.521	0.624	0.775	283.354	25.288	0.759	0.861	193.983	30.189	0.877	0.933	119.254	2368.555
McpTC	20.178	0.524	0.759	329.922	26.444	0.774	0.876	168.717	36.690	0.949	0.968	55.841	2069.351
PSTNN	20.807	0.561	0.784	292.246	32.978	0.916	0.952	75.418	39.795	0.974	0.986	35.032	260.059
SMFLRTC	35.743	0.959	0.975	54.765	39.430	0.978	0.986	36.030	42.505	0.988	0.992	25.403	1082.246
KBRTC	28.898	0.863	0.924	127.082	38.852	0.973	0.984	43.495	44.365	0.991	0.995	22.041	1080.037
ESPTC	28.516	0.828	0.904	132.219	34.232	0.924	0.955	70.417	38.884	0.968	0.982	41.825	1792.766
FTNN	26.691	0.777	0.877	157.785	30.658	0.877	0.927	101.872	35.174	0.942	0.964	62.267	1749.613
WSTNN	37.083	0.968	0.981	50.027	42.199	0.987	0.992	28.408	47.582	0.995	0.997	15.496	1575.438
NWSTNN	39.234	0.970	0.984	37.972	44.997	0.989	0.994	20.735	51.224	0.997	0.998	10.308	2885.440
FFMTC	<b>41.317</b>	<b>0.982</b>	<b>0.990</b>	<b>29.417</b>	<b>46.388</b>	<b>0.993</b>	<b>0.996</b>	<b>17.143</b>	<b>51.980</b>	<b>0.997</b>	<b>0.999</b>	<b>8.951</b>	<b>3045.806</b>

TABLE 6  
The PSNR, SSIM, and FSIM values output by observed and the five utilized TRPCA methods for HSI.

HSI	NL	0.2			0.4			Time(s)
	Method	PSNR	SSIM	FSIM	PSNR	SSIM	FSIM	
Pavia City Center	Observed	11.8104	0.1254	0.5656	8.7975	0.0480	0.4223	0.0000
	SNN	30.7029	0.9324	0.9501	27.5276	0.8406	0.8878	18.3582
	TNN	46.2184	0.9895	0.9923	38.4297	0.9744	0.9830	45.8733
	3DTNN	46.2144	0.9986	0.9989	40.8729	0.9954	0.9961	65.3882
	3DLogTNN	57.4007	0.9998	0.9998	44.6775	0.9973	0.9980	108.9973
	FFMTRPCA	<b>60.3023</b>	<b>0.9999</b>	<b>0.9999</b>	<b>45.9924</b>	<b>0.9983</b>	<b>0.9986</b>	<b>166.6786</b>
Washington DC	Observed	11.4303	0.1222	0.5527	8.4179	0.0478	0.4117	0.0000
	SNN	31.4787	0.9279	0.9509	28.2191	0.8489	0.9022	41.6687
	TNN	43.8989	0.9922	0.9943	35.8265	0.9533	0.9737	104.9230
	3DTNN	50.7842	0.9996	0.9996	42.2630	0.9933	0.9952	214.2376
	3DLogTNN	51.3655	0.9995	0.9996	47.5463	0.9986	0.9989	269.4383
	FFMTRPCA	<b>54.1785</b>	<b>0.9998</b>	<b>0.9998</b>	<b>49.9167</b>	<b>0.9994</b>	<b>0.9994</b>	<b>368.1501</b>
Houston	Observed	10.9201	0.0412	0.4359	7.9205	0.0136	0.2824	0.0000
	SNN	34.7662	0.9114	0.9312	32.1612	0.8531	0.8866	35.3139
	TNN	46.5744	0.9915	0.9943	40.4294	0.9639	0.9815	100.3306
	3DTNN	49.0261	0.9980	0.9988	46.7518	0.9963	0.9973	181.8898
	3DLogTNN	57.2123	0.9994	0.9996	48.8178	0.9972	0.9981	246.6725
	FFMTRPCA	<b>59.5381</b>	<b>0.9994</b>	<b>0.9996</b>	<b>51.2677</b>	<b>0.9981</b>	<b>0.9986</b>	<b>414.5798</b>

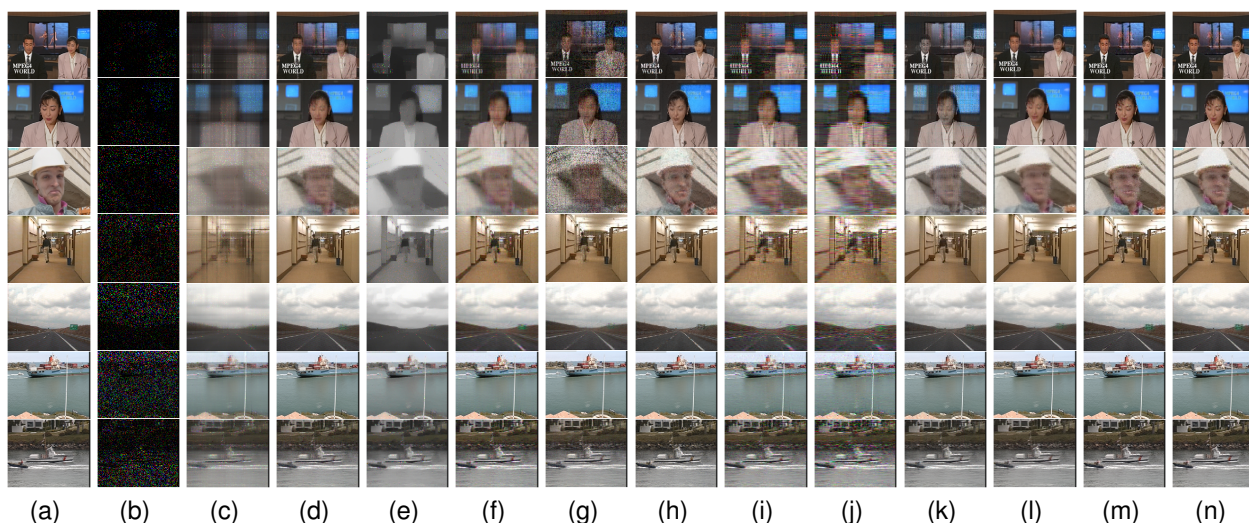


Fig. 5. (a) Original image. (b) Observed image. (c) HaLRTC. (d) TNN. (e) LRTCTV-I. (f) McpTC. (g) PSTNN. (h) SMFLRTC. (i) KBRTC. (j) ESPTC. (k) FTNN. (l) WSTNN. (m) NWSTNN. (n) FFMTC. SR: top 3 rows is 5%, middle 2 rows is 10% and last 2 rows is 20%. The rows of CVs are in order: the 7th frame of news, the 14th frame of akiyo, the 21st frame of foreman, the 28th frame of hall, the 35th frame of highway, the 42nd frame of container, and the 49th frame of coastguard.

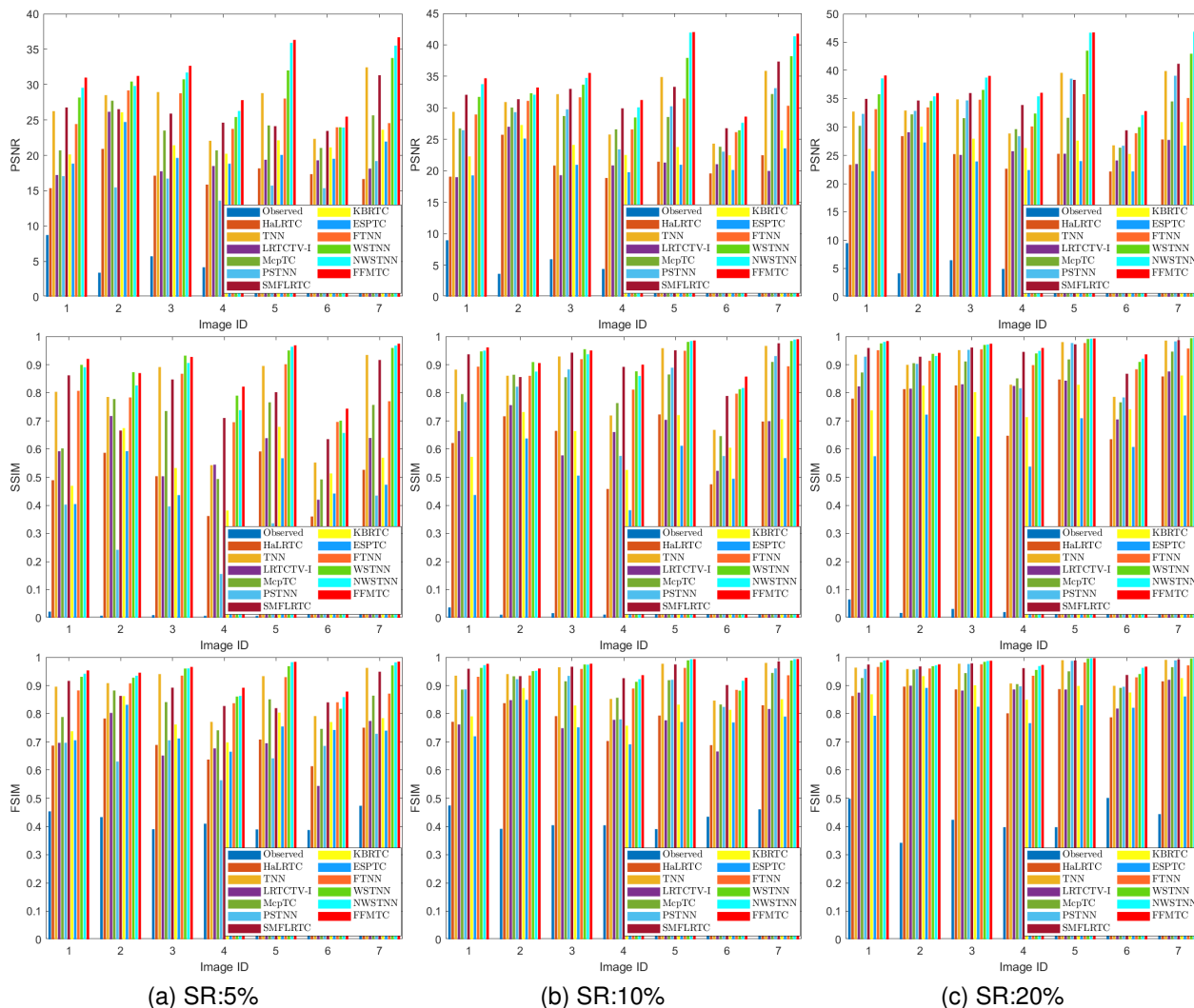


Fig. 6. Comparison of the PSNR values (top), SSIM values (middle) and FSIM values (bottom) obtained by FFMTC and the state-of-the-art methods on 32 MSIs. SR: (a)5%, (b)10%, (c)20%.

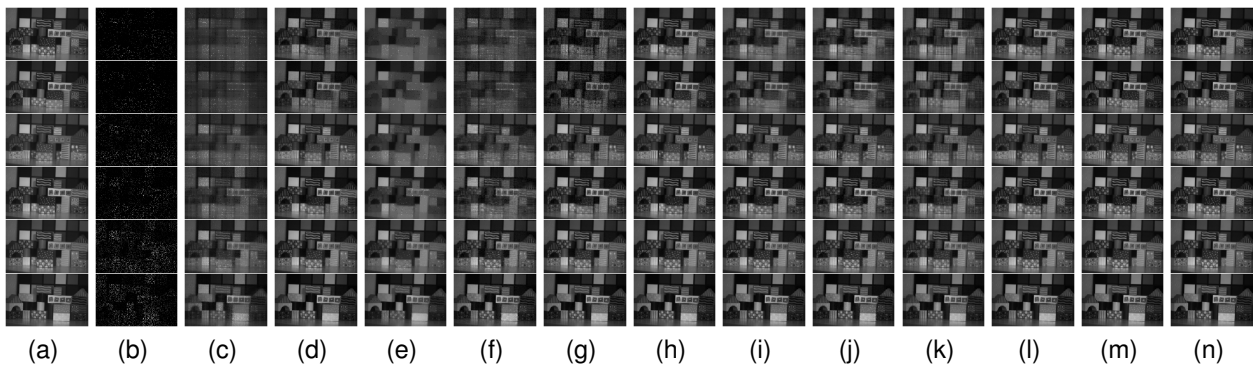


Fig. 7. (a) Original image. (b) Observed image. (c) HaLRTC. (d) TNN. (e) LRTCTV-I. (f) McpTC. (g) PSTNN. (h) SMFLRTC. (i) KBRTC. (j) ESPTC. (k) FTNN. (l) WSTNN. (m) NWSTNN. (n) FFMTC. SR: top 2 rows is 5%, middle 2 rows is 10% and last 2 rows is 20%. The number of frame and band corresponding to each row are as follows: 7 band and 25 frame, 11 band and 16 frame, 3 band and 28 frame, 8 band and 25 frame, 5 band and 27 frame, 14 band and 8 frame.

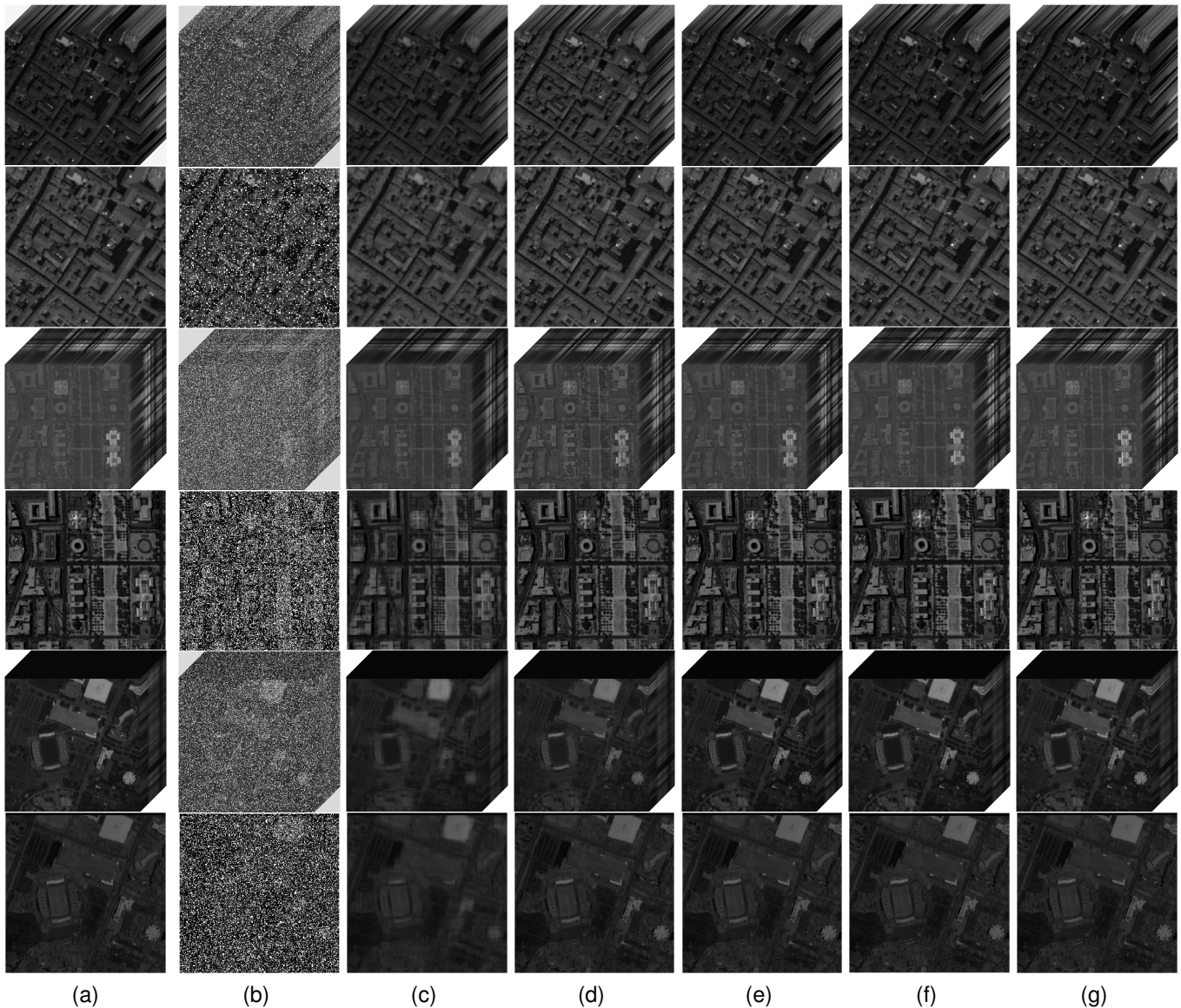


Fig. 8. (a) Original image. (b) Noise image. (c) SNN. (d) TNN. (e) 3DTNN. (f) 3DLogTNN. (g) FFMTRPCA. NL: top 2 rows is 0.2, bottom 4 rows is 0.4. HSIs are as follows: Pavia, Washington, Houston. The bands are in order: 30 band of Pavia, 110 band of Washington, 40 band of Houston.

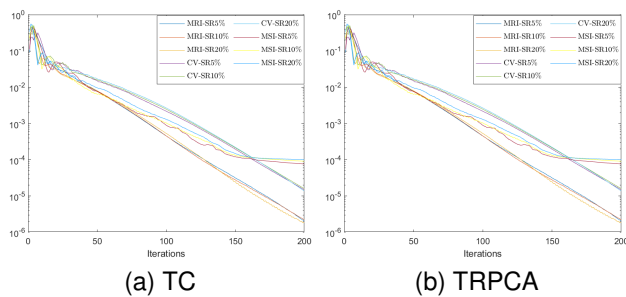


Fig. 9. The convergence behaviours of Algorithm 2, with respect to different sampling rates. The convergence behaviours of Algorithm 3, with respect to different noise level.

in the figure 9. It can be seen that our algorithm converges stably, and the convergence speed is also quite fast.

## 7 CONCLUSION

In this paper, a new tensor sparse measure is proposed, and FFM-based LRTC model and FFM-based TRPCA model are presented for LRTC and TRPCA problems. This sparse measure is more comprehensive in describing the features of tensors, which is a basic guarantee for our method to get ideal results. A large number of real data experiments verify that the proposed method is quite effective and highly efficient. Compared with other state-of-the-art methods, our method is optimal in the experiment of multiple data. How to construct a more appropriate tensor sparse measure is still the direction we need to think about in the future.

## REFERENCES

- [1] S. Li, R. Dian, L. Fang, and J. M. Bioucas-Dias, "Fusing hyperspectral and multispectral images via coupled sparse tensor factorization," *IEEE Transactions on Image Processing*, vol. 27, no. 8, pp. 4118–4130, 2018.
- [2] X. Fu, W.-K. Ma, J. M. Bioucas-Dias, and T.-H. Chan, "Semibind hyperspectral unmixing in the presence of spectral library mismatches," *IEEE Transactions on Geoscience and Remote Sensing*, vol. 54, no. 9, pp. 5171–5184, 2016.
- [3] J. Xue, Y. Zhao, W. Liao, and J. C.-W. Chan, "Nonlocal low-rank regularized tensor decomposition for hyperspectral image denoising," *IEEE Transactions on Geoscience and Remote Sensing*, vol. 57, no. 7, pp. 5174–5189, 2019.
- [4] J. Xue, Y. Zhao, W. Liao, J. C.-W. Chan, and S. G. Kong, "Enhanced sparsity prior model for low-rank tensor completion," *IEEE Transactions on Neural Networks and Learning Systems*, vol. 31, no. 11, pp. 4567–4581, 2020.
- [5] Y.-M. Huang, H.-Y. Yan, Y.-W. Wen, and X. Yang, "Rank minimization with applications to image noise removal," *Information Sciences*, vol. 429, pp. 147–163, 2018.
- [6] B. Madathil and S. N. George, "Twist tensor total variation regularized-reweighted nuclear norm based tensor completion for video missing area recovery," *Information Sciences*, vol. 423, pp. 376–397, 2018.
- [7] Y. Wang, D. Meng, and M. Yuan, "Sparse recovery: from vectors to tensors," *National Science Review*, vol. 5, no. 5, pp. 756–767, 2018.
- [8] X.-L. Zhao, W.-H. Xu, T.-X. Jiang, Y. Wang, and M. K. Ng, "Deep plug-and-play prior for low-rank tensor completion," *Neurocomputing*, vol. 400, pp. 137–149, 2020.
- [9] H. Zhang, X. Liu, H. Fan, Y. Li, and Y. Ye, "Fast and accurate low-rank tensor completion methods based on qr decomposition and  $l_{\{2,1\}}$  norm minimization," *arXiv preprint arXiv:2108.03002*, 2021.
- [10] J.-H. Yang, X.-L. Zhao, T.-Y. Ji, T.-H. Ma, and T.-Z. Huang, "Low-rank tensor train for tensor robust principal component analysis," *Applied Mathematics and Computation*, vol. 367, p. 124783, 2020.
- [11] T.-X. Jiang, T.-Z. Huang, X.-L. Zhao, T.-Y. Ji, and L.-J. Deng, "Matrix factorization for low-rank tensor completion using framelet prior," *Information Sciences*, vol. 436, pp. 403–417, 2018.
- [12] M. Ding, T.-Z. Huang, T.-Y. Ji, X.-L. Zhao, and J.-H. Yang, "Low-rank tensor completion using matrix factorization based on tensor train rank and total variation," *Journal of Scientific Computing*, vol. 81, no. 2, pp. 941–964, 2019.
- [13] J. Xue, Y. Zhao, W. Liao, and J. Cheung-Wai Chan, "Nonconvex tensor rank minimization and its applications to tensor recovery," *Information Sciences*, vol. 503, pp. 109–128, 2019.
- [14] J. Xue, Y. Zhao, W. Liao, and J. Cheung-Wai Chan, "Total variation and rank-1 constraint rpca for background subtraction," *IEEE Access*, vol. 6, pp. 49 955–49 966, 2018.
- [15] I. Kajo, N. Kamel, Y. Ruichek, and A. S. Malik, "Svd-based tensor-completion technique for background initialization," *IEEE Transactions on Image Processing*, vol. 27, no. 6, pp. 3114–3126, 2018.
- [16] W. Cao, Y. Wang, J. Sun, D. Meng, C. Yang, A. Cichocki, and Z. Xu, "Total variation regularized tensor rpca for background subtraction from compressive measurements," *IEEE Transactions on Image Processing*, vol. 25, no. 9, pp. 4075–4090, 2016.
- [17] W. Wei, L. Yi, Q. Xie, Q. Zhao, D. Meng, and Z. Xu, "Should we encode rain streaks in video as deterministic or stochastic?" in *2017 IEEE International Conference on Computer Vision (ICCV)*, 2017, pp. 2535–2544.
- [18] M. Li, Q. Xie, Q. Zhao, W. Wei, S. Gu, J. Tao, and D. Meng, "Video rain streak removal by multiscale convolutional sparse coding," in *2018 IEEE/CVF Conference on Computer Vision and Pattern Recognition*, 2018, pp. 6644–6653.
- [19] Q. Zhao, L. Zhang, and A. Cichocki, "Bayesian cp factorization of incomplete tensors with automatic rank determination," *IEEE Transactions on Pattern Analysis and Machine Intelligence*, vol. 37, no. 9, pp. 1751–1763, 2015.
- [20] T. Yokota, N. Lee, and A. Cichocki, "Robust multilinear tensor rank estimation using higher order singular value decomposition and information criteria," *IEEE Transactions on Signal Processing*, vol. 65, no. 5, pp. 1196–1206, 2017.
- [21] E. J. Candès, X. Li, Y. Ma, and J. Wright, "Robust principal component analysis?" *Journal of the ACM (JACM)*, vol. 58, no. 3, pp. 1–37, 2011.
- [22] E. J. Candès, M. B. Wakin, and S. P. Boyd, "Enhancing sparsity by reweighted  $l_1$  minimization," *Journal of Fourier analysis and applications*, vol. 14, no. 5, pp. 877–905, 2008.
- [23] F. De La Torre and M. J. Black, "A framework for robust subspace learning," *International Journal of Computer Vision*, vol. 54, no. 1, pp. 117–142, 2003.
- [24] S. Gu, L. Zhang, W. Zuo, and X. Feng, "Weighted nuclear norm minimization with application to image denoising," *Proceedings of the IEEE conference on computer vision and pattern recognition*, pp. 2862–2869, 2014.
- [25] D. Meng and F. De la Torre, "Robust matrix factorization with unknown noise," *2013 IEEE International Conference on Computer Vision*, pp. 1337–1344, 2013.
- [26] F. Parvaresh, H. Vikalo, S. Misra, and B. Hassibi, "Recovering sparse signals using sparse measurement matrices in compressed dna microarrays," *IEEE Journal of Selected Topics in Signal Processing*, vol. 2, no. 3, pp. 275–285, 2008.
- [27] J. Wright, A. Ganesh, S. R. Rao, Y. Peng, and Y. Ma, "Robust principal component analysis: Exact recovery of corrupted low-rank matrices via convex optimization." *NIPS*, vol. 58, pp. 289–298, 2009.
- [28] Q. Zhao, D. Meng, Z. Xu, W. Zuo, and L. Zhang, "Robust principal component analysis with complex noise," *International conference on machine learning*, pp. 55–63, 2014.
- [29] E. Acar, D. M. Dunlavy, T. G. Kolda, and M. Mørup, "Scalable tensor factorizations for incomplete data," *Chemometrics and Intelligent Laboratory Systems*, vol. 106, no. 1, pp. 41–56, 2011.
- [30] P. Tichavský, A.-H. Phan, and A. Cichocki, "Numerical cp decomposition of some difficult tensors," *Journal of Computational and Applied Mathematics*, vol. 317, pp. 362–370, 2017.
- [31] Y.-F. Li, K. Shang, and Z.-H. Huang, "Low tucker rank tensor recovery via admm based on exact and inexact iteratively reweighted algorithms," *Journal of Computational and Applied Mathematics*, vol. 331, pp. 64–81, 2018.
- [32] X. Li, M. K. Ng, G. Cong, Y. Ye, and Q. Wu, "Mr-ntd: Manifold regularization nonnegative Tucker decomposition for tensor data dimension reduction and representation," *IEEE Transactions on*

- Neural Networks and Learning Systems*, vol. 28, no. 8, pp. 1787–1800, 2017.
- [33] Z. Zhang, G. Ely, S. Aeron, N. Hao, and M. Kilmer, “Novel methods for multilinear data completion and de-noising based on tensor-svd,” *2014 IEEE Conference on Computer Vision and Pattern Recognition*, pp. 3842–3849, 2014.
- [34] C. J. Hillar and L.-H. Lim, “Most tensor problems are np-hard,” *Journal of the ACM (JACM)*, vol. 60, no. 6, pp. 1–39, 2013.
- [35] K. Braman, “Third-order tensors as linear operators on a space of matrices,” *Linear Algebra and its Applications*, vol. 433, no. 7, pp. 1241–1253, 2010.
- [36] M. E. Kilmer and C. D. Martin, “Factorization strategies for third-order tensors,” *Linear Algebra and its Applications*, vol. 435, no. 3, pp. 641–658, 2011.
- [37] M. E. Kilmer, K. Braman, N. Hao, and R. C. Hoover, “Third-order tensors as operators on matrices: A theoretical and computational framework with applications in imaging,” *SIAM Journal on Matrix Analysis and Applications*, vol. 34, no. 1, pp. 148–172, 2013.
- [38] Y.-B. Zheng, T.-Z. Huang, X.-L. Zhao, T.-X. Jiang, T.-Y. Ji, and T.-H. Ma, “Tensor n-tubal rank and its convex relaxation for low-rank tensor recovery,” *Information Sciences*, vol. 532, pp. 170–189, 2020.
- [39] T. G. Kolda and B. W. Bader, “Tensor decompositions and applications,” *SIAM review*, vol. 51, no. 3, pp. 455–500, 2009.
- [40] M. E. Kilmer and C. D. Martin, “Factorization strategies for third-order tensors,” *Linear Algebra and its Applications*, vol. 435, no. 3, pp. 641–658, 2011.
- [41] C. Lu, J. Feng, Y. Chen, W. Liu, Z. Lin, and S. Yan, “Tensor robust principal component analysis with a new tensor nuclear norm,” *IEEE Transactions on Pattern Analysis and Machine Intelligence*, vol. 42, no. 4, pp. 925–938, 2020.
- [42] T. G. Kolda and B. W. Bader, “Tensor decompositions and applications,” *SIAM review*, vol. 51, no. 3, pp. 455–500, 2009.
- [43] J. Liu, P. Musialski, P. Wonka, and J. Ye, “Tensor completion for estimating missing values in visual data,” *IEEE Transactions on Pattern Analysis and Machine Intelligence*, vol. 35, no. 1, pp. 208–220, 2013.
- [44] Y. Fu, J. Gao, D. Tien, Z. Lin, and X. Hong, “Tensor lrr and sparse coding-based subspace clustering,” *IEEE Transactions on Neural Networks and Learning Systems*, vol. 27, no. 10, pp. 2120–2133, 2016.
- [45] H. Kasai and B. Mishra, “Low-rank tensor completion: a riemannian manifold preconditioning approach,” *International conference on machine learning*, pp. 1012–1021, 2016.
- [46] C. Li, L. Guo, Y. Tao, J. Wang, L. Qi, and Z. Dou, “Yet another Schatten norm for tensor recovery,” *International conference on neural information processing*, pp. 51–60, 2016.
- [47] C. Mu, B. Huang, J. Wright, and D. Goldfarb, “Square deal: Lower bounds and improved relaxations for tensor recovery,” *International conference on machine learning*, pp. 73–81, 2014.
- [48] Q. Xie, Q. Zhao, D. Meng, and Z. Xu, “Kronecker-basis-representation based tensor sparsity and its applications to tensor recovery,” *IEEE Transactions on Pattern Analysis and Machine Intelligence*, vol. 40, no. 8, pp. 1888–1902, 2018.
- [49] C. Lu, C. Zhu, C. Xu, S. Yan, and Z. Lin, “Generalized singular value thresholding,” *Proceedings of the AAAI Conference on Artificial Intelligence*, vol. 29, no. 1, 2015.
- [50] S. Gu, L. Zhang, W. Zuo, and X. Feng, “Weighted nuclear norm minimization with application to image denoising,” *Proceedings of the IEEE conference on computer vision and pattern recognition*, pp. 2862–2869, 2014.
- [51] N. Srebro and T. Jaakkola, “Weighted low-rank approximations,” *Proceedings of the 20th International Conference on Machine Learning (ICML-03)*, pp. 720–727, 2003.
- [52] H. Wang, F. Zhang, J. Wang, T. Huang, J. Huang, and X. Liu, “Generalized nonconvex approach for low-tubal-rank tensor recovery,” *IEEE Transactions on Neural Networks and Learning Systems*, pp. 1–15, 2021.
- [53] L. Chen, X. Jiang, X. Liu, and Z. Zhou, “Robust low-rank tensor recovery via nonconvex singular value minimization,” *IEEE Transactions on Image Processing*, vol. 29, pp. 9044–9059, 2020.
- [54] R. Tibshirani, “Regression shrinkage and selection via the lasso: a retrospective,” *Journal of the Royal Statistical Society: Series B (Statistical Methodology)*, vol. 73, no. 3, pp. 273–282, 2011.
- [55] Z. Wang, A. Bovik, H. Sheikh, and E. Simoncelli, “Image quality assessment: from error visibility to structural similarity,” *IEEE Transactions on Image Processing*, vol. 13, no. 4, pp. 600–612, 2004.
- [56] L. Zhang, L. Zhang, X. Mou, and D. Zhang, “Fsim: A feature similarity index for image quality assessment,” *IEEE Transactions on Image Processing*, vol. 20, no. 8, pp. 2378–2386, 2011.
- [57] L. Wald, *Data fusion: definitions and architectures: fusion of images of different spatial resolutions*. Presses des MINES, 2002.
- [58] X. Li, Y. Ye, and X. Xu, “Low-rank tensor completion with total variation for visual data inpainting,” *Proceedings of the AAAI Conference on Artificial Intelligence*, vol. 31, no. 1, 2017.
- [59] Z. Zhang and S. Aeron, “Exact tensor completion using t-svd,” *IEEE Transactions on Signal Processing*, vol. 65, no. 6, pp. 1511–1526, 2017.
- [60] T.-X. Jiang, T.-Z. Huang, X.-L. Zhao, and L.-J. Deng, “Multi-dimensional imaging data recovery via minimizing the partial sum of tubal nuclear norm,” *Journal of Computational and Applied Mathematics*, vol. 372, p. 112680, 2020.
- [61] T.-X. Jiang, M. K. Ng, X.-L. Zhao, and T.-Z. Huang, “Framelet representation of tensor nuclear norm for third-order tensor completion,” *IEEE Transactions on Image Processing*, vol. 29, pp. 7233–7244, 2020.
- [62] Y.-B. Zheng, T.-Z. Huang, X.-L. Zhao, T.-X. Jiang, T.-H. Ma, and T.-Y. Ji, “Mixed noise removal in hyperspectral image via low-fibered-rank regularization,” *IEEE Transactions on Geoscience and Remote Sensing*, vol. 58, no. 1, pp. 734–749, 2019.
- [63] W. Cao, Y. Wang, C. Yang, X. Chang, Z. Han, and Z. Xu, “Folded-concave penalization approaches to tensor completion,” *Neurocomputing*, vol. 152, pp. 261–273, 2015.
- [64] Y.-B. Zheng, T.-Z. Huang, T.-Y. Ji, X.-L. Zhao, T.-X. Jiang, and T.-H. Ma, “Low-rank tensor completion via smooth matrix factorization,” *Applied Mathematical Modelling*, vol. 70, pp. 677–695, 2019.
- [65] A. Mian and R. Hartley, “Hyperspectral video restoration using optical flow and sparse coding,” *Optics express*, vol. 20, no. 10, pp. 10 658–10 673, 2012.
- [66] D. Goldfarb and Z. Qin, “Robust low-rank tensor recovery: Models and algorithms,” *SIAM Journal on Matrix Analysis and Applications*, vol. 35, no. 1, pp. 225–253, 2014.